

Nonlinear static analysis of composite beams with piezoelectric actuator patches using the Refined Zigzag Theory

Original

Nonlinear static analysis of composite beams with piezoelectric actuator patches using the Refined Zigzag Theory / Ascione, Alessia; Gherlone, Marco; Orifici, Adrian C.. - In: COMPOSITE STRUCTURES. - ISSN 0263-8223. - ELETTRONICO. - 282:115018(2022), pp. 1-18. [10.1016/j.compstruct.2021.115018]

Availability:

This version is available at: 11583/2945672 since: 2021-12-16T14:47:45Z

Publisher:

Elsevier

Published

DOI:10.1016/j.compstruct.2021.115018

Terms of use:

This article is made available under terms and conditions as specified in the corresponding bibliographic description in the repository

Publisher copyright

(Article begins on next page)

Nonlinear static analysis of composite beams with piezoelectric actuator patches using the Refined Zigzag Theory

Alessia Ascione^{a,b,*}, Marco Gherlone^a, Adrian C. Orifici^b

^aDepartment of Mechanical and Aerospace Engineering - Politecnico di Torino, Corso Duca degli Abruzzi 24, 10129 Torino, Italy

^bSchool of Engineering, RMIT University, GPO Box 2476, Melbourne, Victoria 3000, Australia

Abstract

Piezoelectric actuators have been highly successful in a wide range of structural control applications. As such, there is an ongoing need for rapid and accurate structural analysis techniques, particularly for highly heterogeneous composite materials and accounting for the actuator as a patch.

Here, a new model based on the Refined Zigzag Theory (RZT) formulation that includes geometric nonlinearities is proposed for buckling, postbuckling and nonlinear static response analyses of geometrically imperfect composite beams with piezoelectric actuators.

Both the analytical and the finite element (FE) formulation are presented for symmetrically and non-symmetrically laminated beams. The FE approximation is further generalised to the case of beams with geometric discontinuities to model composite beams with piezoelectric actuator patches. The new RZT model is numerically verified through comparisons to Abaqus solutions for buckling and postbuckling analyses and for the geometrically nonlinear response to an applied voltage of geometrically imperfect composite beams with piezoelectric actuator patches.

This work presents a new model for composite beams with piezoelectric actuators and confirms the remarkable advantages of RZT in terms of accuracy and computational efficiency also for challenging nonlinear analyses, where the RZT computational time is generally less than half the time required by the FE commercial code.

Keywords: Refined Zigzag Theory, MFC PZT actuators, Geometrically nonlinear analysis, Composite beams, Buckling analysis, Geometric imperfections

1. Introduction

Over the past fifty years, the use of advanced composite materials in the aerospace industry has significantly increased to meet the demand for better performances and lighter weight. A way to further enhance the performances of aerospace composite structures is to use piezoelectric patch transducers.

One of the most widely used piezoelectric materials is the lead zirconate titanate (PZT) based piezoceramic. Monolithic piezoceramic wafers were used as the initial configuration of piezoceramic actuators, but the brittle nature and the relatively high stiffness of the material resulted in very poorly conformable devices, especially when applied to curved or irregular surfaces [1]. In addition, the actuation capability and the strain energy density of the monolithic piezoceramics were not sufficient for structural control and shape changing applications. For these reasons, subsequent research works focused on improving the properties of PZT-based actuators by changing their structural arrangement to create piezoelectric fibre composites.

The Active Fibre Composite (AFC) represented the most promising development of piezoelectric composites for struc-

tural control applications. AFC actuators were made of unidirectionally aligned PZT fibres embedded in a polymer matrix and sandwiched between an interdigitated electrode pattern [2]. The presence of the polymer matrix allowed the use of very thin piezoelectric fibres, which reduced the bending stiffness and increased the conformability of the actuator. Compared to monolithic piezoceramics, AFC had also a higher strength and significantly higher strain energy density and in-plane directional actuation strain due to the use of the interdigitated electrode (IDE). AFC actuators were also more suitable for controlling lightweight structures and thin membranes because of the lower mass and the improved conformability [3]. However, AFC had two major disadvantages: the extremely high manufacturing cost, due to the manual handling and alignment of the piezoelectric fibres, and the attenuation of the electric field due to the small contact area between the IDE and the circular piezoelectric rods. These problems were overcome by the Macro Fiber Composite (MFC) developed by NASA in 1999. The MFC piezo-composite actuator retained the same essential characteristics of AFC, but the PZT fibres had a rectangular cross section and were machined by cutting low-cost piezoceramic wafers using a computer controlled dicing saw [4]. The automatic process of fibre manufacturing and handling significantly reduced the production costs of MFC. In addition, the rectangular shape of the fibre cross section maximised the area

*Corresponding author. Tel: +44 7387356147.

Email address: alessia.ascione@hotmail.com (Alessia Ascione)

directly in contact with the IDE, thus optimising the electric field transfer to the fibres. As a result, MFC was not only characterised by an excellent mechanical conformability, but it also exhibited superior actuation performances for a considerably lower production cost than AFC.

Since their development, a primary application of piezo-composite actuators was the vibration and noise suppression in aerospace structures [5–8]. In addition, the enhanced actuation performance of the piezo-composite actuators led to their use for structural control and shape-changing. In particular, they became very attractive for controlling the stability of aerospace structures, like for multi-stable morphing structures, where PZT actuators could be used as a method to drive the transition between multiple equilibrium states [9–11], or to further enhance the behaviour of aircraft structures designed to work in post-buckling conditions by controlling the response to compressive loads [12, 13].

Because of the great success of these devices, a significant amount of work was carried out by researchers for predicting the behaviour of structures with integrated piezoelectric actuator patches. In the case of composite structures, the coupling between the mechanical and the electric field introduced by the piezo-actuator was an additional challenge to the well-known difficulties of modelling structures with heterogeneous material properties.

Many authors employed either the Bernoulli-Euler Theory (BET) or the Timoshenko Beam Theory (TBT) for modelling beams with piezoelectric actuators, also for composite laminated beams [14–20]. The simplicity of the BET and the TBT formulations result in very efficient analyses, but both theories are not generally accurate for composites. The reason is that they assume a planar beam cross-section after the deformation, whereas composite beams exhibit a discontinuity in the slope of the axial displacements through the thickness at the interface between two consecutive layers. As a consequence, the strains and the stresses calculated by BET and the TBT for composite beams can be significantly inaccurate.

The High-Shear Deformation Theories (HSDTs) and the Layer-Wise Theories (LWTs) were developed to correctly model the through-the-thickness distribution of the axial displacements in composite laminates and beams. LWTs were generally more accurate than HSDTs, especially for highly heterogeneous material laminations, but they had a number of kinematic variables proportional to the number of layers in the laminate. The Zigzag Theories (ZZTs), a subclass of the LWTs, were created with the intent to have formulations with a constant number of kinematic variables, as with HSDTs, but accurate enough also for highly heterogeneous material properties. One of the Zigzag Theories, the Refined Zigzag Theory [21], was proven to be very efficient and accurate for composite laminated and highly heterogeneous sandwich beams compared to other popular ZZTs [22]. Many analytical formulations based on HSDTs, LWTs and ZZTs were extended to the analysis of structures with piezoelectric actuators [23–28]. However, the majority of these models considered the piezoelectric actuators as continuous layers in the composite structure, whereas the commercially available piezoelectric actuators with the best ac-

tuation performances are patch actuators.

The presence of patch actuators applied to only a small portion of a beam surface increases the complexity of the analytical model because the thickness and material properties change along the beam length. The use of Finite Element (FE) commercial codes is the most versatile way for performing structural analyses: FE commercial codes allow the modelling of complex geometries in detail and guarantee highly accurate results. However, a generally accurate model of composite structures using commercial FE programs like ABAQUS requires the use of two- or three-dimensional finite elements, even in case of a simple beam geometries, because the one-dimensional finite elements are based on TBT [29]. Consequently, the computational cost for performing accurate analyses of composite beams using FE commercial codes is higher than that required by analytical formulations based on one-dimensional finite elements. This can be a big drawback when complex analyses, like the study of the stability and the nonlinear postbuckling analysis of composite beams, are performed. Moreover, the presence of piezoelectric actuators in a composite beam increases the complexity of the model (number of degrees of freedom) causing a further increase in the computational cost.

For this reason, there is a need to create a new method for the buckling and postbuckling analysis of composite beams with PZT actuators which is sufficiently accurate as FE commercial codes but more efficient. Among the theories developed ad-hoc for composite beams, the Refined Zigzag Theory is a promising tool to satisfy the requirements of both accuracy and efficiency. In [30], RZT was extended to the buckling and postbuckling analysis of composite and sandwich beams, also including the beam geometric imperfections, and the results showed that RZT was as accurate as FE commercial codes with a computational cost comparable to TBT. The accuracy of RZT was also experimentally demonstrated for predicting the static bending [31], the natural frequencies [32] and the critical buckling loads [33] of highly heterogeneous sandwich beams.

To the authors' knowledge, RZT was employed for the analysis of composite structures with piezoelectric actuators only in [34], where an analytical formulation was proposed for the vibration analysis of functionally graded carbon nanotube reinforced composite microplates with continuous piezoelectric layers.

The present work aims to provide a new, accurate and efficient method to evaluate the nonlinear static response, the buckling loads and the postbuckling behaviour of composite beams with piezoelectric actuators, either as continuous layers or discrete patches. The method has been formulated to be valid for both symmetric and non-symmetric material laminations and for any number of piezoelectric layers or patches.

The nonlinear formulation of RZT for initially imperfect beams has been extended to include piezoelectric actuators. RZT C^0 -beam elements [35] have been employed to derive the corresponding finite element formulation, that has been further extended to model beams with geometric interfaces, like those introduced by actuator patches on the external surfaces of the beam. The procedure to solve the nonlinear equilibrium equations employing the Newton-Raphson method has been pre-

sented for both cases of incremental mechanical forces and incremental electrical forces.

Subsequently, the method has been numerically verified through comparisons to Abaqus solutions for five composite multilayer beams with either symmetric or non-symmetric material laminations and piezoelectric actuator patches bonded on the beam external surfaces. The buckling loads, the nonlinear response to an axial-compressive load and the nonlinear response to a voltage applied to the piezoelectric actuators have been calculated for each beam in simply supported boundary conditions. A highly-detailed finite element model of each beam has been realised in Abaqus employing three-dimensional finite elements and the same analyses have been performed using the commercial code.

The comparisons between the RZT and the Abaqus solutions have proven the remarkable accuracy and computational efficiency of the proposed method, making it a very convenient alternative to FE commercial codes for performing nonlinear analyses of piezo-composite beams.

2. Analytical model

In this section, the basic assumptions of the Refined Zigzag Theory (RZT) for beams are briefly reviewed extending the nonlinear formulation of the theory for imperfect beams [30] to the case of composite beams with piezoelectric actuator layers. The Principle of Virtual Work (PVW) for electro-mechanical fields is formulated according to RZT to derive the nonlinear equilibrium equations of geometrically imperfect composite beams with piezoelectric actuator layers in terms of the RZT kinematic variables.

2.1. Nonlinear RZT for composite beams with piezoelectric layers: basic assumptions

In this new formulation of the RZT for beams, the beam lamination is constituted of N orthotropic material layers, including piezoelectric materials, with the orthotropy axes corresponding to the coordinates x and y of the Cartesian reference system of the beam, (x, y, z) . The coordinate $x \in [x_a, x_b]$ corresponds to the beam longitudinal axis and the coordinate $z \in [-h, h]$ corresponds to the beam thickness (see Fig.[1]). The length of the beam is L and the cross-sectional area $A = 2h \times b$ lays in the (y, z) plane. Each layer of the lamination is denoted with a superscript (k) and has a thickness $2h^{(k)}$. The centroidal axis of the beam presents an initial (stress-free) transversal deviation from a straight configuration and it is described by the function $w^*(x)$.

In Fig.[1], $p^b(x)$ and $p^t(x)$, $q^b(x)$ and $q^t(x)$ are, respectively, the distributed transverse loads and the distributed axial loads applied to the bottom ($z = -h$) and the top ($z = +h$) surface of the beam. Concentrated forces are applied to the end cross-sections and they are the axial forces, (T_{xa}, T_{xb}) , and the transverse-shear tractions, (T_{za}, T_{zb}) . In addition, a voltage $V^{(k)}$ is applied to the k th layer made of piezoelectric material. Only planar deformations in the (x, z) plane are considered under the assigned load system.

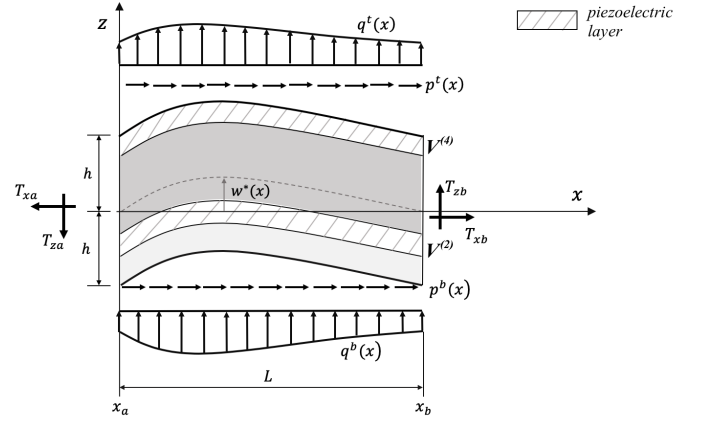


Figure 1: Notation for beam geometry and applied loads.

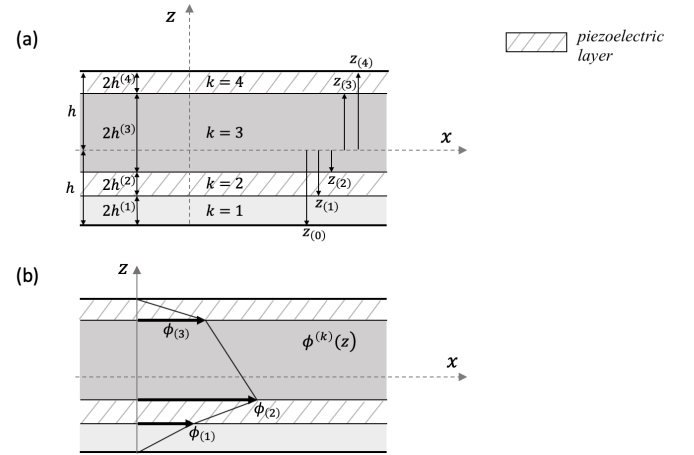


Figure 2: Through-thickness layer notation and zigzag function of the Refined Zigzag Theory for a four-layered piezo-composite laminate: (a) layer notation and (b) zigzag function.

The orthogonal components of the RZT displacement vector, \mathbf{s} , are the displacements in the directions of the x - and z -axis, $u_x^{(k)}$ and u_z respectively [35]. The transverse displacement $u_z \equiv w$ is assumed to be uniform along the beam thickness, thus it is independent of the k th layer characteristics. The kinematic variables of the theory are the uniform axial displacement, $u(x)$, the deflection, $w(x)$, the average cross-sectional (bending) rotation, $\theta(x)$, and the zigzag rotation, $\psi(x)$, which is the variable introduced to model the through-the-thickness zigzag trend of the axial displacement. The four kinematic variables are the component of the vector \mathbf{u} ; in matrix form, the RZT displacement vector is then

$$\mathbf{s} \equiv \begin{Bmatrix} u_x^{(k)}(x, z) \\ u_z(x, z) \end{Bmatrix} = \begin{bmatrix} 1 & 0 & z & \phi^{(k)} \\ 0 & 1 & 0 & 0 \end{bmatrix} \begin{Bmatrix} u(x) \\ w(x) \\ \theta(x) \\ \psi(x) \end{Bmatrix} \equiv \mathbf{Z}_u \mathbf{u}, \quad (1)$$

where $\phi^{(k)}$ is the zigzag function, which is piecewise linear and C^0 continuous along the thickness. The zigzag function $\phi^{(k)}$ vanishes on the top and the bottom beam surfaces ($\phi_{(0)} =$

$\phi_{(N)} = 0$) whereas the values at the internal interfaces between two consecutive layers are defined by

$$\phi_{(j)} = \phi_{(j-1)} + 2h^{(j)}\beta^{(j)}, \quad j = 1, \dots, N-1, \quad (2)$$

where the subscript of $\phi_{(i)}$ ($i = 0, \dots, N$) indicates the layer interface, as shown in Fig.[2]. The slope of $\phi^{(k)}$ in each layer is $\beta^{(k)}$ and it can be calculated from the material properties of the layers as

$$\beta^{(k)} = \frac{G}{G_{xz}^{(k)}} - 1, \quad k = 1, \dots, N, \quad (3)$$

where $G_{xz}^{(k)}$ is the transverse-shear modulus of the k -th layer and G is

$$G = \frac{2h}{\int_{-h}^h (1/G_{xz}^{(k)}) dz} = \frac{2h}{\sum_{k=1}^N (h^{(k)}/G_{xz}^{(k)})}. \quad (4)$$

In case of a non-symmetric lamination with one of the external layers of a transverse-shear rigidity weaker than the adjacent one, the external layer behaviour is driven by the internal layer and, consequently, the slope of the axial displacement function, $u(x, z)$, along z is continuous at the interface. This means that the slope of the zigzag function has to be the same in the two consecutive layers. In [22], Gherlone proved that the correct implementation of the RZT in this particular case is obtained assuming that the transverse-shear modulus of the inner layer is the same as the external weaker layer for defining the zigzag function.

In [30], the RZT was extended considering the von Kármán nonlinear kinematic equations particularised to beam structures with geometric imperfections,

$$\begin{aligned} \epsilon_x &= u_{x,x} + \frac{1}{2}u_{z,x}^2 + u_{z,x}w_{,x}^*, \\ \gamma_{xz} &= \frac{1}{2}(u_{x,z} + u_{z,x}). \end{aligned} \quad (5)$$

Substituting the derivatives of the displacement components of Eq.[1] in Eq.[5], the RZT nonlinear axial strain, $\epsilon_x^{(k)}$, and shear strain, $\gamma_{xz}^{(k)}$, are obtained:

$$\begin{aligned} \epsilon_x^{(k)} &= u_{,x} + z\theta_{,x} + \phi^{(k)}\psi_{,x} + \frac{1}{2}w_{,x}^2 + w_{,x}w_{,x}^*, \\ &= \mathbf{Z}_\epsilon^{(k)}\boldsymbol{\omega} + \frac{1}{2}\boldsymbol{\omega}^T\mathbf{H}\boldsymbol{\omega} + \boldsymbol{\omega}^{*T}\boldsymbol{\omega}, \\ \gamma_{xz}^{(k)} &= w_{,x} + \theta + \beta^{(k)}\psi \\ &= \mathbf{Z}_\gamma^{(k)}\boldsymbol{\omega}. \end{aligned} \quad (6)$$

The vectors $\boldsymbol{\omega}$ and $\boldsymbol{\omega}^*$ contain, respectively, the derivative with respect to the x -coordinate of the kinematic variables of the theory and of the initial imperfection function, $w^*(x)$,

$$\boldsymbol{\omega} \equiv [u_{,x} \quad w_{,x} \quad \theta \quad \psi \quad \theta_{,x} \quad \psi_{,x}]^T, \quad (7)$$

$$\boldsymbol{\omega}^* \equiv [0 \quad w_{,x}^* \quad 0 \quad 0 \quad 0 \quad 0]^T. \quad (8)$$

The matrices \mathbf{H} , $\mathbf{Z}_\epsilon^{(k)}$ and $\mathbf{Z}_\gamma^{(k)}$ are defined in Appendix A.

Making the hypotheses that the beam exhibits a plane-stress behavior in the (x, z) plane and the transverse normal stress $\sigma_z^{(k)}$ is negligibly small compared to the axial and transverse-shear stresses, the constitutive relations of the beam for a linearly coupled electro-mechanical field are

$$\begin{aligned} \sigma_x^{(k)} &= E_x^{(k)}\epsilon_x^{(k)} - e_{31}^{(k)}\Xi_z^{(k)}, \\ \tau_{xz}^{(k)} &= G_{xz}^{(k)}\gamma_{xz}^{(k)}, \end{aligned} \quad (9)$$

$$D_z^{(k)} = e_{31}^{(k)}\epsilon_x^{(k)} + \chi_{33}^{(k)}\Xi_z^{(k)}, \quad (10)$$

where $E_x^{(k)}$ is the axial modulus, $e_{31}^{(k)}$ the piezoelectric stress coefficient, $D_z^{(k)}$ is the component along z of the electric displacement vector and $\chi_{33}^{(k)}$ the dielectric permittivity of the material of the k th layer. All the mechanical and electrical properties are assumed to be constant in time and within each layer.

2.2. The Principle of Virtual Work for electro-mechanical systems

The PVW for electro-mechanical systems can be formulated as the equality of the virtual variation of the electrical enthalpy, δH_E , and the virtual work of the external forces and electrical charges, δL [36]:

$$\delta H_E = \delta L. \quad (11)$$

By definition, the electrical enthalpy is related to the internal energy, U , and to the work of the internal charges, U_E , as follows [36]:

$$H_E = U - U_E, \quad (12)$$

and the virtual variation of H_E is

$$\delta H_E = \int_V \delta \boldsymbol{\epsilon}^T \boldsymbol{\sigma} dV - \int_V \delta \boldsymbol{\Xi}^T \mathbf{D} dV, \quad (13)$$

where the quantities $\boldsymbol{\epsilon}$ and $\boldsymbol{\sigma}$ are the strain and stress tensors, and $\boldsymbol{\Xi}^{(k)}$ and $\mathbf{D}^{(k)}$ are the electric field vector and the electric displacement vector (see Appendix B for more details about the characteristics of the piezoelectric layers and the definition of $\boldsymbol{\Xi}^{(k)}$ and $\mathbf{D}^{(k)}$).

In this application, a voltage source is assumed as electric power supplier for the piezoelectric actuator layers. This means that the electric potential on each electrode of the piezoelectric layer, and thus the electric field $\Xi_z^{(k)}$ in the layer, are prescribed. Consequently, the virtual variation $\delta \Xi_z^{(k)}$ vanishes and

$$\delta H_E = \int_{x_a}^{x_b} \int_A [\delta \epsilon_x^{(k)} \sigma_x^{(k)} + \delta \gamma_{xz}^{(k)} \tau_{xz}^{(k)}] dA dx. \quad (14)$$

In addition, the virtual work of the external forces and electrical charges is

$$\delta L = \delta L_m + \delta L_E, \quad (15)$$

but $\delta L_E = 0$ because it depends on the virtual variation of the electric potential which is prescribed. Then, δL corresponds to δL_m , and for the load system represented in Fig.[1],

$$\begin{aligned} \delta L_m = & \int_{x_a}^{x_b} \left[p^b \delta u_x^{(1)}(-h) + p^t \delta u_x^{(N)}(+h) + q^b \delta u_z^{(1)}(-h) + \right. \\ & \left. + q^t \delta u_z^{(N)}(+h) \right] dx - \int_A \left[T_{xa} \delta u_x^{(k)}(x_a, z) + T_{za} \delta u_z^{(k)}(x_a, z) \right] dA + \\ & + \int_A \left[T_{xb} \delta u_x^{(k)}(x_b, z) + T_{zb} \delta u_z^{(k)}(x_b, z) \right] dA. \end{aligned} \quad (16)$$

Then, the general formulation of the PVW based on the nonlinear RZT for imperfect beams with piezoelectric actuator layers corresponds to that presented in [30] for composite beams without piezoelectric layers.

The mechanical internal forces and moments are defined as

$$\begin{aligned} [N_x, M_x, M_\phi] &\equiv \int_A (1, z, \phi^{(k)}) \sigma_x^{(k)} dA, \\ [V_x, V_\phi] &\equiv \int_A (1, \beta^{(k)}) \tau_{xz}^{(k)} dA. \end{aligned} \quad (17)$$

The nonlinear constitutive equations are obtained substituting the strains of Eqs.[6] in Eqs.[9] and then the stresses in Eqs.[17]; in matrix form

$$\mathbf{R} = \Lambda \omega + \bar{\Lambda} \left(\frac{1}{2} \omega^T H \omega + \omega^{*T} \omega \right) - \mathbf{F}^{ind}, \quad (18)$$

where the vector $\mathbf{R} \equiv [N_x \ V_x \ V_\phi \ M_x \ M_\phi]^T$ contains the stress resultants. In this new formulation for beams with piezoelectric actuator layers, the vector \mathbf{F}^{ind} appears in the constitutive equations, which contains the induced axial force and moments due to the piezoelectric actuation,

$$\begin{aligned} \mathbf{F}^{ind} &\equiv [N_x^{ind} \ 0 \ 0 \ M_x^{ind} \ M_\phi^{ind}]^T \\ &\equiv \int_A e_{31}^{(k)} \Xi_z^{(k)} [1, 0, 0, z, \phi^{(k)}]^T dA. \end{aligned} \quad (19)$$

The equilibrium equations in terms of displacement components can be obtained making use of Eqs.[12-16] and Eq.[18]:

$$\begin{aligned} A_{11} \left[u_{,xx} + \left(\frac{1}{2} w_{,x}^2 + w_{,x} w_{,x}^* \right) \right] + B_{12} \theta_{,xx} + B_{13} \psi_{,xx} + \bar{p} - N_{x,x}^{ind} &= 0, \\ \left\{ A_{11} \left(u_{,x} + \frac{1}{2} w_{,x}^2 + w_{,x} w_{,x}^* \right) + B_{12} \theta_{,x} + B_{13} \psi_{,x} - N_x^{ind} \right\}_{,x} &+ \\ + \bar{G} A (w_{,xx} + \theta_{,x}) + (G - \bar{G}) A \psi_{,x} + \bar{q} &= 0, \\ B_{12} \left[u_{,xx} + \left(\frac{1}{2} w_{,x}^2 + w_{,x} w_{,x}^* \right) \right] + D_{11} \theta_{,xx} + D_{12} \psi_{,xx} - (G - \bar{G}) A \psi &+ \\ - \bar{G} A (w_{,x} + \theta) + \bar{m} - M_{x,x}^{ind} &= 0, \\ B_{13} \left[u_{,xx} + \left(\frac{1}{2} w_{,x}^2 + w_{,x} w_{,x}^* \right) \right] + D_{12} \theta_{,xx} + D_{22} \psi_{,xx} - (\bar{G} - G) A \psi &+ \\ - (G - \bar{G}) A (w_{,x} + \theta) - M_{\phi,x}^{ind} &= 0. \end{aligned} \quad (20)$$

The equilibrium equations in Eq.[20] differ from the case of beams without piezoelectric actuator layers for the presence of the derivative with respect to the x -coordinate of the induced axial force and moments.

The electric field in the k th piezoelectric layer can be expressed as the ratio of the applied voltage, $V^{(k)}$, to the layer thickness, $2h^{(k)}$,

$$\Xi_z^{(k)} = \frac{V^{(k)}}{2h^{(k)}}, \quad (21)$$

thus the induced resultant force and moments of Eq.[19] can be expressed as

$$[N_x^{ind}, 0, 0, M_x^{ind}, M_\phi^{ind}]^T = \int_A \frac{e_{31}^{(k)}}{2h^{(k)}} V^{(k)} [1, 0, 0, z, \phi^{(k)}]^T dA. \quad (22)$$

The electrical quantities $e_{31}^{(k)}$ and $V^{(k)}$ are constant within the layer so they can be taken out of the integral. Defining the k th layer electrical stiffness coefficients per unit of voltage as

$$[a_E^{(k)}, d_E^{(k)}, c_E^{(k)}] \equiv b \frac{e_{31}^{(k)}}{2h^{(k)}} \int_{z^-}^{z^+} (1, z, \phi^{(k)}) dz, \quad (23)$$

then Eq.[22] becomes

$$[N_x^{ind}, 0, 0, M_x^{ind}, M_\phi^{ind}]^T = \sum_{k=1}^N [a_E^{(k)}, 0, 0, d_E^{(k)}, c_E^{(k)}]^T V^{(k)}. \quad (24)$$

3. Finite element formulation of the RZT for geometrically imperfect beams with piezoelectric actuators

In this section, the finite element approximation is introduced to derive the FE expression of δH_E and δL based on RZT beam finite elements. The FE equilibrium equation is derived and it is shown how it can be simplified for particular boundary and loading conditions. Subsequently, the FE model is extended to

the case of beams with physical interfaces, as when piezoelectric actuator patches are locally bonded to the external surfaces of the beam. Finally, the Newton-Raphson method is implemented for solving the nonlinear FE equilibrium equation for either mechanical or electrical loads.

3.1. General formulation

The matrix expression of the virtual variation of the electrical enthalpy is obtained substituting Eqs.[6] and Eqs.[9] in Eq.[14]:

$$\begin{aligned}
\delta H_E = & \int_{x_a}^{x_b} \int_A \left[\delta \omega^T \mathbf{Z}_\epsilon^{(k)T} E_x^{(k)} \mathbf{Z}_\epsilon^{(k)} \omega \right] dA dx + \\
& + \frac{1}{2} \int_{x_a}^{x_b} \int_A \left[\delta \omega^T \mathbf{Z}_\epsilon^{(k)T} E_x^{(k)} \omega^T \mathbf{H} \omega \right] dA dx + \\
& + \int_{x_a}^{x_b} \int_A \left[\delta \omega^T \mathbf{Z}_\epsilon^{(k)T} E_x^{(k)} \omega^{*T} \omega \right] dA dx + \\
& + \int_{x_a}^{x_b} \int_A \left[\delta \omega^T \mathbf{H} \omega E_x^{(k)} \mathbf{Z}_\epsilon^{(k)} \omega \right] dA dx + \\
& + \int_{x_a}^{x_b} \int_A \left[\delta \omega^T \mathbf{H} \omega E_x^{(k)} \left(\frac{1}{2} \omega^T \mathbf{H} \omega \right) \right] dA dx + \\
& + \int_{x_a}^{x_b} \int_A \left[\delta \omega^T \mathbf{H} \omega E_x^{(k)} (\omega^{*T} \omega) \right] dA dx + \\
& + \int_{x_a}^{x_b} \int_A \left[\delta \omega^T \omega^* E_x^{(k)} \mathbf{Z}_\epsilon^{(k)} \omega \right] dA dx + \\
& + \int_{x_a}^{x_b} \int_A \left[\delta \omega^T \omega^* E_x^{(k)} \left(\frac{1}{2} \omega^T \mathbf{H} \omega \right) \right] dA dx + \\
& + \int_{x_a}^{x_b} \int_A \left[\delta \omega^T \omega^* E_x^{(k)} (\omega^{*T} \omega) \right] dA dx + \\
& - \int_{x_a}^{x_b} \int_A \left[\delta \omega^T \mathbf{Z}_\epsilon^{(k)T} e_{31}^{(k)} \Xi_z^{(k)} \right] dA dx + \\
& - \int_{x_a}^{x_b} \int_A \left[\delta \omega^T \mathbf{H} \omega e_{31}^{(k)} \Xi_z^{(k)} \right] dA dx + \\
& - \int_{x_a}^{x_b} \int_A \left[\delta \omega^T \omega^* e_{31}^{(k)} \Xi_z^{(k)} \right] dA dx + \\
& + \int_{x_a}^{x_b} \int_A \left[\delta \omega^T \mathbf{Z}_\gamma^{(k)T} G_{xz}^{(k)} \mathbf{Z}_\gamma^{(k)} \omega \right] dA dx.
\end{aligned} \tag{25}$$

The *anisoparametric-constrained* interpolation is employed for the approximation of the RZT kinematic variables within the finite element. The corresponding C^0 -continuous beam finite element has two nodes and four degrees of freedom per node, as shown in Fig.[3] and the kinematic variables approximation is the following:

$$\mathbf{u} = \begin{Bmatrix} u(x) \\ w(x) \\ \vartheta(x) \\ \psi(x) \end{Bmatrix} \simeq \mathbf{N} \mathbf{u}^e, \tag{26}$$

where \mathbf{N} is the shape function matrix and \mathbf{u}^e is the vector containing the degrees of freedom of the element,

$$\mathbf{u}^e \equiv [u_1 \quad w_1 \quad \theta_1 \quad \psi_1 \quad u_2 \quad w_2 \quad \theta_2 \quad \psi_2]^T. \tag{27}$$

The complete derivation of the anisoparametric-constrained finite element based on the RZT for beams and further details on the constraint condition can be found in [35].

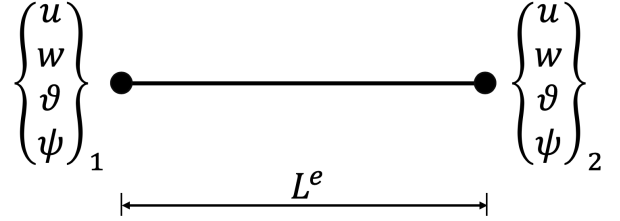


Figure 3: Two-node constrained anisoparametric element based on the Refined Zigzag Theory for beams.

The vector of the derivative of the kinematic variables, ω , can be approximated as

$$\omega \simeq \mathbf{B}^e \mathbf{u}^e, \tag{28}$$

where the matrix \mathbf{B}^e contains the derivative of the shape functions with respect to the x coordinate.

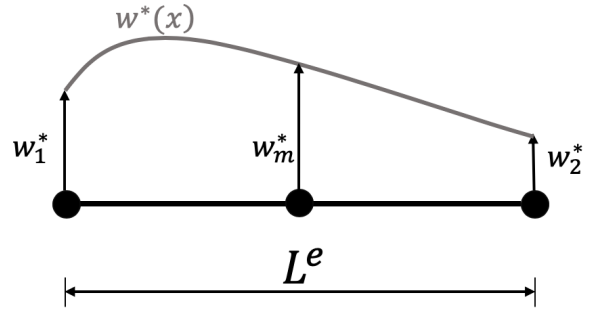


Figure 4: Parabolic approximation of the initial imperfection in the finite element.

Introducing the vector \mathbf{u}^{*e} , containing the values of the geometric imperfection at the finite element edges, w_1^* and w_2^* , and at the mid-point, w_m^* ,

$$\mathbf{u}^{*e} \equiv [w_1^* \quad w_m^* \quad w_2^*]^T, \tag{29}$$

the approximation of the initial imperfection function $w^*(x)$ within the finite element (see Fig.[4]) is

$$w^*(x) \simeq \mathbf{N}^* \mathbf{u}^{*e}. \tag{30}$$

The finite element approximation of the vector ω^* is then

$$\omega^* \simeq \mathbf{B}^{*e} \mathbf{u}^{*e}, \tag{31}$$

where \mathbf{B}^{*e} contains the derivative of the functions of \mathbf{N}^* with respect to the x coordinate.

The definition of the shape function matrices, \mathbf{N} and \mathbf{N}^* , and the definition of \mathbf{B}^e and \mathbf{B}^{*e} can be found in Appendix A.

Substituting Eq.[28] and Eq.[31] in Eq.[25] the finite element approximation of the electrical enthalpy can be obtained,

$$\begin{aligned}
\delta H_E^e \approx & \delta \mathbf{u}^{eT} \cdot \left\{ \left[\int_{x_a}^{x_b} \mathbf{B}^{eT} \left(\int_A \mathbf{Z}_\epsilon^{(k)T} E_x^{(k)} \mathbf{Z}_\epsilon^{(k)} dA \right) \mathbf{B}^e dx + \right. \right. \\
& + \int_{x_a}^{x_b} \mathbf{B}^{eT} \left(\int_A \mathbf{Z}_\gamma^{(k)T} G_{xz}^{(k)} \mathbf{Z}_\gamma^{(k)} dA \right) \mathbf{B}^e dx + \\
& + \frac{1}{2} \int_{x_a}^{x_b} \mathbf{B}^{eT} \left(\int_A \mathbf{Z}_\epsilon^{(k)T} E_x^{(k)} dA \right) \mathbf{u}^{*eT} \mathbf{B}^{*eT} \mathbf{H} \mathbf{B}^e dx + \\
& + \int_{x_a}^{x_b} \mathbf{B}^{eT} \left(\int_A \mathbf{Z}_\epsilon^{(k)T} E_x^{(k)} dA \right) \mathbf{u}^{*eT} \mathbf{B}^{*eT} \mathbf{B}^e dx + \\
& + \frac{1}{2} \int_{x_a}^{x_b} \mathbf{B}^{eT} \mathbf{H} \mathbf{B}^e \mathbf{u}^e \left(\int_A E_x^{(k)} dA \right) \mathbf{u}^{*eT} \mathbf{B}^{*eT} \mathbf{H} \mathbf{B}^e dx + \\
& + \int_{x_a}^{x_b} \mathbf{B}^{eT} \mathbf{H} \mathbf{B}^e \mathbf{u}^e \left(\int_A E_x^{(k)} \mathbf{Z}_\epsilon^{(k)} dA \right) \mathbf{B}^e dx + \\
& + \int_{x_a}^{x_b} \mathbf{B}^{eT} \mathbf{H} \mathbf{B}^e \mathbf{u}^e \left(\int_A E_x^{(k)} dA \right) \mathbf{u}^{*eT} \mathbf{B}^{*eT} \mathbf{B}^e dx + \\
& + \int_{x_a}^{x_b} \mathbf{B}^{eT} \mathbf{B}^{*e} \mathbf{u}^{*e} \left(\int_A E_x^{(k)} dA \right) \mathbf{u}^{*eT} \mathbf{B}^{*eT} \mathbf{B}^e dx + \\
& + \int_{x_a}^{x_b} \mathbf{B}^{eT} \mathbf{B}^{*e} \mathbf{u}^{*e} \left(\int_A E_x^{(k)} \mathbf{Z}_\epsilon^{(k)} dA \right) \mathbf{B}^e dx + \\
& + \frac{1}{2} \int_{x_a}^{x_b} \mathbf{B}^{eT} \mathbf{B}^{*e} \mathbf{u}^{*e} \left(\int_A E_x^{(k)} dA \right) \mathbf{u}^{*eT} \mathbf{B}^{*eT} \mathbf{H} \mathbf{B}^e dx + \\
& - \int_{x_a}^{x_b} \left(\int_A e_{31}^{(k)} \Xi_z^{(k)} dA \right) \mathbf{B}^{eT} \mathbf{H} \mathbf{B}^e \mathbf{u}^e dx \Big] \cdot \mathbf{u}^e + \\
& - \int_{x_a}^{x_b} \mathbf{B}^{eT} \left(\int_A \mathbf{Z}_\epsilon^{(k)T} e_{31}^{(k)} \Xi_z^{(k)} dA \right) dx + \\
& \left. - \int_{x_a}^{x_b} \left(\int_A e_{31}^{(k)} \Xi_z^{(k)} dA \right) \mathbf{B}^{eT} \mathbf{B}^{*e} dx \cdot \mathbf{u}^{*e} \right\}. \tag{32}
\end{aligned}$$

In order to express the integrals containing the electric terms in a matrix form, a vector \mathbf{V}_P^e (dimension $N \times 1$) is defined with the elements corresponding to the values V_P^{ek} of the voltage applied in k th layer of the finite element ($V_P^{ek} = 0$ if the layer is not made of piezoelectric material or if the applied voltage is zero):

$$\mathbf{V}_P^e \equiv \begin{bmatrix} V_P^{e1} & \dots & V_P^{ek} & \dots & V_P^{eN} \end{bmatrix}^T. \tag{33}$$

Making the following simplifications:

$$\int_A e_{31}^{(k)} \Xi_z^{(k)} dA \equiv N_x^{inde}, \quad \int_A \mathbf{Z}_\epsilon^{(k)T} e_{31}^{(k)} \Xi_z^{(k)} dA \equiv \mathbf{Z}_P^e \mathbf{V}_P^e, \tag{34}$$

the matrix form of the electrical enthalpy is then

$$\begin{aligned}
\delta H_E^e \approx & \delta \mathbf{u}^{eT} \cdot \left\{ \left[\int_{x_a}^{x_b} \mathbf{B}^{eT} \left(\int_A \mathbf{Z}_\epsilon^{(k)T} E_x^{(k)} \mathbf{Z}_\epsilon^{(k)} dA \right) \mathbf{B}^e dx + \right. \right. \\
& + \int_{x_a}^{x_b} \mathbf{B}^{eT} \left(\int_A \mathbf{Z}_\gamma^{(k)T} G_{xz}^{(k)} \mathbf{Z}_\gamma^{(k)} dA \right) \mathbf{B}^e dx + \\
& + \frac{1}{2} \int_{x_a}^{x_b} \mathbf{B}^{eT} \mathbf{Z}_N^e \mathbf{u}^{*eT} \mathbf{B}^{*eT} \mathbf{H} \mathbf{B}^e dx + \\
& + \int_{x_a}^{x_b} \mathbf{B}^{eT} \mathbf{Z}_N^e \mathbf{u}^{*eT} \mathbf{B}^{*eT} \mathbf{B}^e dx + \\
& + \frac{1}{2} \int_{x_a}^{x_b} \mathbf{B}^{eT} \mathbf{H} \mathbf{B}^e \mathbf{u}^e A_{11}^e \mathbf{u}^{*eT} \mathbf{B}^{*eT} \mathbf{H} \mathbf{B}^e dx + \\
& + \int_{x_a}^{x_b} \mathbf{B}^{eT} \mathbf{H} \mathbf{B}^e \mathbf{u}^e \mathbf{Z}_N^e \mathbf{B}^e dx + \\
& + \int_{x_a}^{x_b} \mathbf{B}^{eT} \mathbf{H} \mathbf{B}^e \mathbf{u}^e A_{11}^e \mathbf{u}^{*eT} \mathbf{B}^{*eT} \mathbf{B}^e dx + \\
& + \int_{x_a}^{x_b} \mathbf{B}^{eT} \mathbf{B}^{*e} \mathbf{u}^{*e} A_{11}^e \mathbf{u}^{*eT} \mathbf{B}^{*eT} \mathbf{B}^e dx + \\
& + \int_{x_a}^{x_b} \mathbf{B}^{eT} \mathbf{B}^{*e} \mathbf{u}^{*e} \mathbf{Z}_N^e \mathbf{B}^e dx + \\
& + \frac{1}{2} \int_{x_a}^{x_b} \mathbf{B}^{eT} \mathbf{B}^{*e} \mathbf{u}^{*e} A_{11}^e \mathbf{u}^{*eT} \mathbf{B}^{*eT} \mathbf{H} \mathbf{B}^e dx + \\
& - N_x^{inde} \int_{x_a}^{x_b} \mathbf{B}^{eT} \mathbf{H} \mathbf{B}^e dx \Big] \cdot \mathbf{u}^e - \int_{x_a}^{x_b} \mathbf{B}^{eT} dx \cdot \mathbf{Z}_P^e \mathbf{V}_P^e + \\
& \left. - N_x^{inde} \int_{x_a}^{x_b} \mathbf{B}^{eT} \mathbf{B}^{*e} dx \cdot \mathbf{u}^{*e} \right\}, \tag{35}
\end{aligned}$$

where the matrices \mathbf{Z}_P^e and \mathbf{Z}_N^e are defined in Appendix A. The FE approximation of the electrical enthalpy can be further simplified introducing the following stiffness matrices:

$$\mathbf{K}^e \equiv \int_{x_a}^{x_b} \mathbf{B}^{eT} \mathbf{D} \mathbf{B}^e dx, \tag{36}$$

$$\bar{\mathbf{K}}_{GI}^e(\mathbf{u}^e) \equiv \int_{x_a}^{x_b} \mathbf{B}^{eT} \mathbf{H} \mathbf{B}^e \mathbf{u}^e \mathbf{Z}_N^e \mathbf{B}^e dx, \tag{37}$$

$$\bar{\mathbf{K}}_{GII}^e(\mathbf{u}^e) \equiv \int_{x_a}^{x_b} \mathbf{B}^{eT} \mathbf{H} \mathbf{B}^e \mathbf{u}^e A_{11}^e \mathbf{u}^{*eT} \mathbf{B}^{*eT} \mathbf{H} \mathbf{B}^e dx, \tag{38}$$

$$\bar{\mathbf{K}}_{GM}^e(\mathbf{u}^e, \mathbf{u}^{*e}) \equiv \int_{x_a}^{x_b} \mathbf{B}^{eT} \mathbf{H} \mathbf{B}^e \mathbf{u}^e A_{11}^e \mathbf{u}^{*eT} \mathbf{B}^{*eT} \mathbf{B}^e dx, \tag{39}$$

$$\mathbf{K}_{GI}^{*e}(\mathbf{u}^{*e}) \equiv \int_{x_a}^{x_b} \mathbf{B}^{eT} \mathbf{B}^{*e} \mathbf{u}^{*e} \mathbf{Z}_N^e \mathbf{B}^e dx, \tag{40}$$

$$\mathbf{K}_{GII}^{*e}(\mathbf{u}^{*e}) \equiv \int_{x_a}^{x_b} \mathbf{B}^{eT} \mathbf{B}^{*e} \mathbf{u}^{*e} A_{11}^e \mathbf{u}^{*eT} \mathbf{B}^{*eT} \mathbf{B}^e dx, \tag{41}$$

$$\mathbf{K}_G^e \equiv \int_{x_a}^{x_b} \mathbf{B}^{eT} \mathbf{H} \mathbf{B}^e dx, \tag{42}$$

$$\mathbf{K}_G^{*e} \equiv \int_{x_a}^{x_b} \mathbf{B}^{eT} \mathbf{B}^{*e} dx, \tag{43}$$

$$\mathbf{K}_P^e \equiv \int_{x_a}^{x_b} \mathbf{B}^{eT} dx \cdot \mathbf{Z}_P^e, \tag{44}$$

where the matrices dependent on \mathbf{u}^e are indicated with an overbar. Substituting Eqs.[36-44] in Eq.[35],

$$\begin{aligned} \delta H_E^e \approx & \delta \mathbf{u}^{eT} \cdot \left[\left(\mathbf{K}^e + \frac{1}{2} \bar{\mathbf{K}}_{\text{GI}}^{eT} + \bar{\mathbf{K}}_{\text{GI}}^e + \mathbf{K}_{\text{GI}}^{*eT} + \mathbf{K}_{\text{GI}}^{*e} + \mathbf{K}_{\text{GII}}^{*e} + \right. \right. \\ & \left. \left. + \frac{1}{2} \bar{\mathbf{K}}_{\text{GII}}^e + \bar{\mathbf{K}}_{\text{GM}}^e + \frac{1}{2} \bar{\mathbf{K}}_{\text{GM}}^{eT} - N_x^{\text{inde}} \mathbf{K}_{\text{G}}^e \right) \cdot \mathbf{u}^e + \right. \\ & \left. - N_x^{\text{inde}} \mathbf{K}_{\text{G}}^{*e} \mathbf{u}^{*e} - \mathbf{K}_{\text{P}}^e \mathbf{V}_{\text{P}}^e \right]. \end{aligned} \quad (45)$$

The virtual work done by the external forces in the finite element approximation corresponds to the product between $\delta \mathbf{u}^e$ and the vector of nodal forces equivalent to the applied mechanical forces, \mathbf{F}^e ,

$$\delta L^e \approx \delta \mathbf{u}^{eT} \mathbf{F}^e. \quad (46)$$

Employing the Principle of Virtual Work (Eq.[11]) in the finite element approximation, the element-based nonlinear-FE equilibrium equation for geometrically imperfect composite beams with piezoelectric actuator layers based on the RZT is obtained:

$$\begin{aligned} \left(\mathbf{K}^e + \frac{1}{2} \bar{\mathbf{K}}_{\text{GI}}^{eT} + \bar{\mathbf{K}}_{\text{GI}}^e + \mathbf{K}_{\text{GI}}^{*eT} + \mathbf{K}_{\text{GI}}^{*e} + \mathbf{K}_{\text{GII}}^{*e} + \frac{1}{2} \bar{\mathbf{K}}_{\text{GII}}^e + \bar{\mathbf{K}}_{\text{GM}}^e + \right. \\ \left. + \frac{1}{2} \bar{\mathbf{K}}_{\text{GM}}^{eT} - N_x^{\text{inde}} \mathbf{K}_{\text{G}}^e \right) \cdot \mathbf{u}^e = \mathbf{F}^e + N_x^{\text{inde}} \mathbf{K}_{\text{G}}^{*e} \mathbf{u}^{*e} + \mathbf{K}_{\text{P}}^e \mathbf{V}_{\text{P}}^e. \end{aligned} \quad (47)$$

The solution of the nonlinear equation identifies the equilibrium condition of the beam for any applied load system and voltage in the piezoelectric layer.

3.2. Constant axial force

For particular boundary and loading conditions the beam axial force is independent of the degrees of freedom and Eq.[47] is reduced to a linear relation. The general definition of the internal axial force is

$$N_x = \int_A \sigma_x dA. \quad (48)$$

The virtual variation of N_x due to a virtual variation of the vector \mathbf{u}^e is

$$\begin{aligned} \delta N_x \approx & \int_A \left[E_x^{(k)} \left(\mathbf{Z}_{\epsilon}^{(k)} \mathbf{B}^e \cdot \delta \mathbf{u}^e + \mathbf{u}^{eT} \mathbf{B}^{eT} \mathbf{H} \mathbf{B}^e \cdot \delta \mathbf{u}^e + \right. \right. \\ & \left. \left. + \mathbf{u}^{*eT} \mathbf{B}^{*eT} \mathbf{B}^e \cdot \delta \mathbf{u}^e \right) \right] dA \\ = & \left(\mathbf{Z}_{\text{N}} \mathbf{B}^e + A_{11}^e \mathbf{u}^{eT} \mathbf{B}^{eT} \mathbf{H} \mathbf{B}^e + A_{11}^e \mathbf{u}^{*eT} \mathbf{B}^{*eT} \mathbf{B}^e \right) \cdot \delta \mathbf{u}^e. \end{aligned} \quad (49)$$

The term linearly dependent on \mathbf{u}^e is indicated as N_{xc} :

$$N_{xc}^e \equiv \mathbf{Z}_{\text{N}}^e \mathbf{B}^e \mathbf{u}^e. \quad (50)$$

The virtual variation of the electrical enthalpy of Eq.[35], after some operations, can be simplified considering that the virtual variation $\delta N_x = 0$ when the axial force is assigned as a consequence of the boundary condition of the beam (e.g. the applied axial force at the supported edge of a simply-supported beam) because N_x is independent of \mathbf{u}^e :

$$\begin{aligned} \delta H_E^e = & \delta \mathbf{u}^{eT} \cdot \left[\int_{x_a}^{x_b} \mathbf{B}^{eT} \left(\int_A \mathbf{Z}_{\epsilon}^{(k)T} E_x^{(k)} \mathbf{Z}_{\epsilon}^{(k)} dA \right) \mathbf{B}^e dx + \right. \\ & + \int_{x_a}^{x_b} \mathbf{B}^{eT} \left(\int_A \mathbf{Z}_{\gamma}^{(k)T} G_{xz}^{(k)} \mathbf{Z}_{\gamma}^{(k)} dA \right) \mathbf{B}^e dx + \\ & + N_{xc}^e \int_{x_a}^{x_b} \mathbf{B}^{eT} \mathbf{H} \mathbf{B}^e dx - N_x^{\text{inde}} \int_{x_a}^{x_b} \mathbf{B}^{eT} \mathbf{H} \mathbf{B}^e dx \Big] \cdot \mathbf{u}^e + \\ & + N_{xc}^e \int_{x_a}^{x_b} \mathbf{B}^{eT} \mathbf{B}^{*e} dx \cdot \mathbf{u}^{*e} - \delta \mathbf{u}^{eT} \cdot \left[\int_{x_a}^{x_b} \mathbf{B}^{eT} dx \cdot \mathbf{Z}_{\text{P}}^e \mathbf{V}_{\text{P}}^e + \right. \\ & \left. + N_x^{\text{inde}} \int_{x_a}^{x_b} \mathbf{B}^{eT} \mathbf{B}^{*e} dx \cdot \mathbf{u}^{*e} \right]. \end{aligned} \quad (51)$$

Substituting Eq.[51] in Eq.[11] and considering Eqs.[36, 42-44,46], the element-based RZT-FE equilibrium equation for a constant axial force is

$$\left[\mathbf{K}^e - \left(N_x^{\text{inde}} - N_{xc}^e \right) \mathbf{K}_{\text{G}}^e \right] \cdot \mathbf{u}^e = \mathbf{F}^e + \left(N_x^{\text{inde}} - N_{xc}^e \right) \mathbf{K}_{\text{G}}^{*e} \mathbf{u}^{*e} + \mathbf{K}_{\text{P}}^e \mathbf{V}_{\text{P}}^e. \quad (52)$$

All the matrices in Eq.[52] are independent of the degrees-of freedom vector, thus, the equation can be solved as a linear equation for any prescribed values of N_x^{inde} and N_{xc}^e . Eq.[52] and, in general, Eq.[47] can be used to find the equilibrium condition of a composite beam for any applied mechanical load and electric voltage. The entire nonlinear load-displacement equilibrium path of axially-compressed beams can be reconstructed by solving the equation for an increasing load from zero to a desired value.

In addition, employing the Euler's method of the adjacent equilibrium configurations[37] in Eq.[52], the stability equation is obtained:

$$\left(\mathbf{K}^e - P_i^e \mathbf{K}_{\text{G}}^e \right) \cdot \hat{\mathbf{u}}_i^e = 0, \quad (53)$$

where the eigenvalues $P_i^e = N_x^{\text{inde}} - N_{xc}^e$ are the buckling loads and the eigenvectors $\hat{\mathbf{u}}_i^e$ are the buckling mode shapes.

3.3. Geometric interface between finite elements

A further generalisation of the formulation is needed to correctly model beams with piezoelectric patches locally bonded to the external surfaces of the beam. The presence of the actuator changes the thickness and the material lamination of the beam in that location. Different material or geometrical properties along the beam length lead to physical interfaces; the two finite elements that share the node at the interface have two different displacement field vectors in that node because of the change in the geometric and material characteristics. This inconsistency can be solved by minimising the difference between the

displacement fields by using a strategy based on the Lagrange multipliers method.

In addition, a geometric discontinuity can be characterised by a misalignment between the half thickness axis of the beam with a consequent offset between the two finite elements.

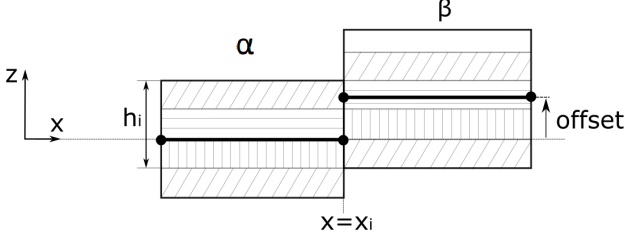


Figure 5: Geometrical interface between the elements α and β .

Considering a physical interface between two finite elements, α and β , at $x = x_i$ (see Fig.[5]), the total potential energy of the system is the sum of the total potential energy of the first element and the total potential energy of the second element:

$$\Pi = \Pi^\alpha + \Pi^\beta. \quad (54)$$

The problem of the beam equilibrium can be solved finding the minimum of the total potential energy subjected to the constraint condition that the work done by fictitious forces on the difference between the two displacement fields at the interface, \mathbf{s}_i^α and \mathbf{s}_i^β , is zero. The physical meaning of this constraint condition is that, since the two elements are joint at the interface, the two displacement fields have to be the same, thus the beam cannot be deformed as if it were split in that location [38].

The total potential energy of the generic finite element j ($j = \alpha, \beta$) is the difference between the strain energy, U^j , and the work done by the external forces L_m^j :

$$\Pi^j = U^j - L_m^j. \quad (55)$$

Considering all the finite element approximation for nonlinear and geometric imperfect beams (for the sake of simplicity, the condition of constant normal force and no electrical contribution is shown), the total potential energy of the element j is

$$\Pi^j = \frac{1}{2} \mathbf{u}^{jT} \mathbf{K}^j \mathbf{u}^j + N_{xc}^j \frac{1}{2} \mathbf{u}^{jT} \mathbf{K}_G^j \mathbf{u}^j + N_{xc}^j \mathbf{u}^{jT} \mathbf{K}_G^{*j} \mathbf{u}^{*j} - \mathbf{u}^{jT} \mathbf{F}^j, \quad (56)$$

thus the total potential energy Π is a function of the degrees of freedom vectors of the two elements, $\Pi = \Pi(\mathbf{u}^\alpha, \mathbf{u}^\beta)$.

The Lagrange function is introduced to transform a constrained minimum problem of the function $\Pi = \Pi(\mathbf{u}^\alpha, \mathbf{u}^\beta)$, into an unconstrained minimum problem of a function, $\Pi_i = \Pi_i(\mathbf{u}^\alpha, \mathbf{u}^\beta, \lambda)$, which depends also on the Lagrange multipliers vector, λ ,

$$\Pi_i = \Pi^\alpha + \Pi^\beta + \int_{A_i} \lambda^T \cdot (\mathbf{s}_i^\alpha - \mathbf{s}_i^\beta) dA. \quad (57)$$

The additional term in Π_i is the fictitious work given by the integral over the interface cross-section, $A_i = h_i \times b$ (the area

shared by the two elements), of the product between the fictitious stresses λ and the difference between the displacement fields of the two elements at the interface.

The function Π_i of Eq.[57], can be then written taking into account also Eq.[1] and Eq.[26]:

$$\begin{aligned} \Pi_i(\mathbf{u}^\alpha, \mathbf{u}^\beta, \lambda) = & \left[\frac{1}{2} \mathbf{u}^{\alpha T} (\mathbf{K}^\alpha + N_{xc}^\alpha \mathbf{K}_G^\alpha) \mathbf{u}^\alpha + N_{xc}^\alpha \mathbf{u}^{\alpha T} \mathbf{K}_G^{*\alpha} \mathbf{u}^{*\alpha} - \mathbf{u}^{\alpha T} \mathbf{F}^\alpha \right] + \\ & + \left[\frac{1}{2} \mathbf{u}^{\beta T} (\mathbf{K}^\beta + N_{xc}^\beta \mathbf{K}_G^\beta) \mathbf{u}^\beta + N_{xc}^\beta \mathbf{u}^{\beta T} \mathbf{K}_G^{*\beta} \mathbf{u}^{*\beta} - \mathbf{u}^{\beta T} \mathbf{F}^\beta \right] + \\ & + \int_{A_i} \lambda^T \cdot (\mathbf{Z}_u^\alpha \mathbf{N}^\alpha(x_i) \mathbf{u}^\alpha - \mathbf{Z}_u^\beta \mathbf{N}^\beta(x_i) \mathbf{u}^\beta) dA. \end{aligned} \quad (58)$$

The Lagrange multipliers vector has two components, λ_u and λ_w , one for each displacement variable. The through-the-thickness distribution of the Lagrange multipliers at the interface is defined using the variables $\bar{\lambda}_{u1}$, $\bar{\lambda}_{u2}$ and $\bar{\lambda}_w$, because a linear distribution is assumed for λ_u , whereas λ_w is constant over the beam cross-section:

$$\lambda = \begin{Bmatrix} \lambda_u \\ \lambda_w \end{Bmatrix} = \begin{bmatrix} N_1^L & N_2^L & 0 \\ 0 & 0 & 1 \end{bmatrix} \begin{Bmatrix} \bar{\lambda}_{u1} \\ \bar{\lambda}_{u2} \\ \bar{\lambda}_w \end{Bmatrix} \equiv \mathbf{N}_\lambda \bar{\lambda}, \quad (59)$$

where N_1^L and N_2^L are the linear Lagrange polynomials defined in AppendixA, but in this case they are function of the thickness coordinate z .

Defining the matrix \mathbf{H}^j for the element j ,

$$\mathbf{H}^j = b^j \int_{h_i} \mathbf{N}_\lambda^T \mathbf{Z}_u^j dz \mathbf{N}^j(x_i), \quad (60)$$

the function Π_i is then

$$\begin{aligned} \Pi_i(\mathbf{u}^\alpha, \mathbf{u}^\beta, \lambda) = & \left[\frac{1}{2} \mathbf{u}^{\alpha T} (\mathbf{K}^\alpha + N_{xc}^\alpha \mathbf{K}_G^\alpha) \mathbf{u}^\alpha + N_{xc}^\alpha \mathbf{u}^{\alpha T} \mathbf{K}_G^{*\alpha} \mathbf{u}^{*\alpha} - \mathbf{u}^{\alpha T} \mathbf{F}^\alpha \right] + \\ & + \left[\frac{1}{2} \mathbf{u}^{\beta T} (\mathbf{K}^\beta + N_{xc}^\beta \mathbf{K}_G^\beta) \mathbf{u}^\beta + N_{xc}^\beta \mathbf{u}^{\beta T} \mathbf{K}_G^{*\beta} \mathbf{u}^{*\beta} - \mathbf{u}^{\beta T} \mathbf{F}^\beta \right] + \\ & + \bar{\lambda}^T \mathbf{H}^\alpha \mathbf{u}^\alpha - \bar{\lambda}^T \mathbf{H}^\beta \mathbf{u}^\beta. \end{aligned} \quad (61)$$

The minimum of the function Π_i can be found solving the following system:

$$\begin{cases} \frac{\partial \Pi_i}{\partial \mathbf{u}^\alpha} = 0, \\ \frac{\partial \Pi_i}{\partial \mathbf{u}^\beta} = 0, \\ \frac{\partial \Pi_i}{\partial \bar{\lambda}} = 0, \end{cases} \quad (62)$$

that is

$$\begin{cases} (\mathbf{K}^\alpha + N_{xc}^\alpha \mathbf{K}_G^\alpha) \mathbf{u}^\alpha + N_{xc}^\alpha \mathbf{K}_G^{*\alpha} \mathbf{u}^{*\alpha} - \mathbf{F}^\alpha + \mathbf{H}^{\alpha T} \bar{\lambda} = 0, \\ (\mathbf{K}^\beta + N_{xc}^\beta \mathbf{K}_G^\beta) \mathbf{u}^\beta + N_{xc}^\beta \mathbf{K}_G^{*\beta} \mathbf{u}^{*\beta} - \mathbf{F}^\beta - \mathbf{H}^{\beta T} \bar{\lambda} = 0, \\ \mathbf{H}^\alpha \mathbf{u}^\alpha - \mathbf{H}^\beta \mathbf{u}^\beta = 0. \end{cases} \quad (63)$$

In matrix form, the degrees of freedom and the Lagrange multipliers can be collected in one vector because they are the variables of the system,

$$\begin{pmatrix} \mathbf{K}^\alpha & \mathbf{0} & \mathbf{H}^{\alpha T} \\ \mathbf{0} & \mathbf{K}^\beta & -\mathbf{H}^{\beta T} \\ \mathbf{H}^\alpha & -\mathbf{H}^\beta & \mathbf{0} \end{pmatrix} + \begin{pmatrix} N_{xc}^\alpha \mathbf{K}_G^{\text{ea}} & \mathbf{0} & \mathbf{0} \\ \mathbf{0} & N_{xc}^\beta \mathbf{K}_G^{\text{eb}} & \mathbf{0} \\ \mathbf{0} & \mathbf{0} & \mathbf{0} \end{pmatrix} \begin{pmatrix} \mathbf{u}^\alpha \\ \mathbf{u}^\beta \\ \lambda \end{pmatrix} = - \begin{pmatrix} N_{xc}^\alpha \mathbf{K}_G^{\text{ea}} & \mathbf{0} \\ \mathbf{0} & N_{xc}^\beta \mathbf{K}_G^{\text{eb}} \\ \mathbf{0} & \mathbf{0} \end{pmatrix} \begin{pmatrix} \mathbf{u}^{\text{ea}} \\ \mathbf{u}^{\text{eb}} \end{pmatrix} + \begin{pmatrix} \mathbf{F}^\alpha \\ \mathbf{F}^\beta \\ \mathbf{0} \end{pmatrix}, \quad (64)$$

that is

$$(\mathbf{K} + \mathbf{K}_{\text{GN}}) \mathbf{u} = -\mathbf{K}_{\text{GN}}^* \mathbf{u}^* + \mathbf{F}, \quad (65)$$

where the vector \mathbf{u} contains both the degrees of freedom of the beam and the Lagrange multipliers variables.

It can be seen that the stiffness matrix \mathbf{K} of a beam with an interface has additional rows and columns for the new degrees of freedom at the interface but also other terms related to the variables of the Lagrange multipliers. The geometric stiffness matrices of the beam, \mathbf{K}_{GN} and \mathbf{K}_{GN}^* , contain the geometric stiffness matrices of each element multiplied by the normal force acting on the element. \mathbf{K}_{GN} , \mathbf{K}_{GN}^* and the vector \mathbf{F} have additional rows and columns of zero-elements corresponding to the Lagrange multipliers variables.

3.4. Newton-Raphson solution of the nonlinear RZT-FE equilibrium equation

The nonlinear equilibrium equation of the whole beam structure is obtained by assembling the element-based matrices and vectors,

$$\begin{pmatrix} \mathbf{K} + \frac{1}{2} \bar{\mathbf{K}}_{\text{GI}}^T + \bar{\mathbf{K}}_{\text{GI}} + \mathbf{K}_{\text{GI}}^{*T} + \mathbf{K}_{\text{GI}}^* + \frac{1}{2} \bar{\mathbf{K}}_{\text{GII}} + \mathbf{K}_{\text{GII}}^* + \bar{\mathbf{K}}_{\text{GM}} + \frac{1}{2} \bar{\mathbf{K}}_{\text{GM}}^T - \mathbf{K}_{\text{GAe}} \end{pmatrix} \cdot \mathbf{u} - \mathbf{F} - \mathbf{K}_{\text{GAe}}^* \mathbf{u}^* - \mathbf{K}_{\text{P}} \mathbf{V}_{\text{P}} = \mathbf{0}, \quad (66)$$

where \mathbf{K}_{GAe} and $\mathbf{K}_{\text{GAe}}^*$ are obtained assembling the matrices $N_x^{\text{inde}} \mathbf{K}_G^{\text{e}}$ and $N_x^{\text{inde}} \mathbf{K}_G^{*\text{e}}$ of each finite element.

The nonlinear RZT-FE equation can be solved employing the incremental-iterative technique based on the Newton-Raphson (N-R) method proposed by Crisfield [39]. Eq.[66] can be written using the vectorial function $\mathbf{g}(\mathbf{u}, \lambda)$ as

$$\mathbf{g}(\mathbf{u}, \lambda) = \mathbf{q}_i(\mathbf{u}, \lambda) - \lambda \mathbf{q}_e = \mathbf{0}, \quad (67)$$

where the vector $\mathbf{q}_i(\mathbf{u}, \lambda)$ is the internal forces vector and it is a function of both the degrees of freedom vector, \mathbf{u} , and the increment factor, λ , whereas \mathbf{q}_e is the external forces vector that increases by λ at each increment.

The definition of \mathbf{q}_i and \mathbf{q}_e depends on the application considered and on the type of load, mechanical or electrical, that increases at each incremental step. In this analysis, the following cases were considered:

1. *Incremental electrical forces:* the voltage vector V_P is gradually increased. At the i th increment, the applied voltage is $V_{Pi} = \lambda_i V_{P1}$, where V_{P1} is the initial reference voltage vector and \mathbf{K}_{GAeI} and $\mathbf{K}_{\text{GAeI}}^*$ the matrices \mathbf{K}_{GAe} and $\mathbf{K}_{\text{GAe}}^*$ for $V_P = V_{P1}$. The vectors \mathbf{q}_i and \mathbf{q}_e are

$$\mathbf{q}_i = \left(\mathbf{K} + \frac{1}{2} \bar{\mathbf{K}}_{\text{GI}}^T + \bar{\mathbf{K}}_{\text{GI}} + \mathbf{K}_{\text{GI}}^{*T} + \mathbf{K}_{\text{GI}}^* + \frac{1}{2} \bar{\mathbf{K}}_{\text{GII}} + \mathbf{K}_{\text{GII}}^* + \frac{1}{2} \bar{\mathbf{K}}_{\text{GM}}^T + \bar{\mathbf{K}}_{\text{GM}} - \lambda \mathbf{K}_{\text{GAeI}} \right) \cdot \mathbf{u}, \quad (68)$$

$$\mathbf{q}_e = \mathbf{K}_{\text{GAeI}}^* \mathbf{u}^* + \mathbf{K}_{\text{P}} \mathbf{V}_{P1}. \quad (69)$$

2. *Incremental mechanical forces:* the initial reference vector of mechanical loads, \mathbf{F}_1 , is gradually increased, thus

$$\mathbf{q}_i = \left(\mathbf{K} + \frac{1}{2} \bar{\mathbf{K}}_{\text{GI}}^T + \bar{\mathbf{K}}_{\text{GI}} + \mathbf{K}_{\text{GI}}^{*T} + \mathbf{K}_{\text{GI}}^* + \frac{1}{2} \bar{\mathbf{K}}_{\text{GII}} + \mathbf{K}_{\text{GII}}^* + \frac{1}{2} \bar{\mathbf{K}}_{\text{GM}}^T + \bar{\mathbf{K}}_{\text{GM}} - \mathbf{K}_{\text{GAe}} \right) \cdot \mathbf{u} - \mathbf{K}_{\text{GAe}}^* \mathbf{u}^* - \mathbf{K}_{\text{P}} \mathbf{V}_{\text{P}}, \quad (70)$$

$$\mathbf{q}_e = \mathbf{F}_1. \quad (71)$$

The Newton-Raphson procedure combines at each step an incremental solution, that is the tangential increment of \mathbf{u} corresponding to the load increment of the step, used as predictive starting solution point (*predictor*), and a certain number of iterations (*corrector*), which find a convergent value of \mathbf{u} for the assigned load. The convergence criterion adopted for both the predictor increments and the corrector iterations is based on the calculation of a parameter indicated as k_c [39],

$$k_c(\mathbf{g}, \mathbf{q}_e) = (\mathbf{g}^T \cdot \mathbf{g})^{0.5} - 0.01 (\mathbf{q}_e^T \cdot \mathbf{q}_e)^{0.5}. \quad (72)$$

The n th predictor increment converges if $k_c(\mathbf{g} = \mathbf{g}^{(n)}, \mathbf{q}_e = \mathbf{q}_e^{(n)}) < 0$ and the i th corrector iteration of the m th predictor increment converges if $k_c(\mathbf{g} = \mathbf{g}_i^{(m)}, \mathbf{q}_e = \mathbf{q}_{ei}^{(m)}) < 0$.

The load factor changes at each increment and it is calculated as

$$\lambda^{(n)} = \lambda^{(n-1)} \sqrt{\frac{I^{ref}}{I^{n-1}}}, \quad (73)$$

where λ^{n-1} is the previous increment factor for which I^{n-1} iterations were required and I^{ref} is a reference number of desired iterations.

Moreover, the N-R procedure requires the calculation of the tangent stiffness matrix, defined as

$$\mathbf{K}_T^e(\mathbf{u}^e) = \frac{d\mathbf{g}^e}{d\mathbf{u}^e}. \quad (74)$$

Eq.[67] shows that only the internal forces vector \mathbf{q}_i depends on the degrees of freedom vector \mathbf{u} , consequently

$$\frac{d\mathbf{g}^e}{d\mathbf{u}^e} = \frac{d\mathbf{q}_i^e}{d\mathbf{u}^e}. \quad (75)$$

The derivative $d\mathbf{q}_i^e/d\mathbf{u}^e$ for both the cases of incremental electrical forces and incremental mechanical forces is (refer to Eqs.[68,70])

$$\begin{aligned} \frac{d\mathbf{q}_i^e}{d\mathbf{u}^e} = & \mathbf{K}^e + \mathbf{K}_{\text{GI}}^{*eT} + \mathbf{K}_{\text{GI}}^{*e} + \frac{1}{2}\bar{\mathbf{K}}_{\text{GII}}^e + \mathbf{K}_{\text{GII}}^{*e} - \mathbf{K}_{\text{GAe}}^e + \\ & + \frac{d}{d\mathbf{u}^e} \left(\frac{1}{2}\bar{\mathbf{K}}_{\text{GI}}^{eT}\mathbf{u}^e + \bar{\mathbf{K}}_{\text{GI}}^e\mathbf{u}^e + \frac{1}{2}\bar{\mathbf{K}}_{\text{GM}}^{eT}\mathbf{u}^e + \bar{\mathbf{K}}_{\text{GM}}^e\mathbf{u}^e \right). \end{aligned} \quad (76)$$

The matrices with the overbar are a function of the degrees of freedom vector \mathbf{u}^e , thus it is useful to define the following matrices obtained by the derivative of the nonlinear terms in Eq.[76]:

$$\frac{d}{d\mathbf{u}^e} [\bar{\mathbf{K}}_{\text{GI}}^e \cdot \mathbf{u}^e] = \bar{\mathbf{K}}_{\text{GI}}^e + \bar{\mathbf{K}}_{\text{GI2}}^e, \quad (77)$$

$$\frac{d}{d\mathbf{u}^e} [\bar{\mathbf{K}}_{\text{GI}}^{eT} \cdot \mathbf{u}^e] = 2\bar{\mathbf{K}}_{\text{GI}}^{eT}, \quad (78)$$

$$\frac{d}{d\mathbf{u}^e} [\bar{\mathbf{K}}_{\text{GII}}^e \cdot \mathbf{u}^e] = 2\bar{\mathbf{K}}_{\text{GII}}^e + \bar{\mathbf{K}}_{\text{GII2}}^e, \quad (79)$$

$$\frac{d}{d\mathbf{u}^e} [\bar{\mathbf{K}}_{\text{GM}}^e \cdot \mathbf{u}^e] = \bar{\mathbf{K}}_{\text{GM}}^e + \bar{\mathbf{K}}_{\text{GM2}}^e, \quad (80)$$

$$\frac{d}{d\mathbf{u}^e} [\bar{\mathbf{K}}_{\text{GM}}^{eT} \cdot \mathbf{u}^e] = 2\bar{\mathbf{K}}_{\text{GM}}^{eT}, \quad (81)$$

where

$$\begin{aligned} \bar{\mathbf{K}}_{\text{GI2}}^e & \equiv \int_{x_a}^{x_b} \mathbf{B}^{eT} \mathbf{H} \mathbf{B}^e \mathbf{Z}_N^e \mathbf{B}^e \mathbf{u}^e dx, \\ \bar{\mathbf{K}}_{\text{GII2}}^e & \equiv A_{11}^e \int_{x_a}^{x_b} \mathbf{B}^{eT} \mathbf{H} \mathbf{B}^e \mathbf{u}^{eT} \mathbf{B}^{eT} \mathbf{H} \mathbf{B}^e \mathbf{u}^e dx, \\ \bar{\mathbf{K}}_{\text{GM2}}^e & \equiv A_{11}^e \int_{x_a}^{x_b} \mathbf{B}^{eT} \mathbf{H} \mathbf{B}^e \mathbf{u}^{*eT} \mathbf{B}^{*eT} \mathbf{B}^e \mathbf{u}^e dx. \end{aligned} \quad (82)$$

The full expression of the tangent stiffness matrix for the nonlinear RZT model is then

$$\begin{aligned} \mathbf{K}_T^e(\mathbf{u}^e) = & \mathbf{K}^e + \bar{\mathbf{K}}_{\text{GI}}^{eT} + \bar{\mathbf{K}}_{\text{GI}}^e + \bar{\mathbf{K}}_{\text{GI2}}^e + \mathbf{K}_{\text{GI}}^{*eT} + \mathbf{K}_{\text{GI}}^{*e} + \bar{\mathbf{K}}_{\text{GII}}^e + \\ & + \frac{1}{2}\bar{\mathbf{K}}_{\text{GII2}}^e + \mathbf{K}_{\text{GII}}^{*e} + \bar{\mathbf{K}}_{\text{GM}}^{eT} + \bar{\mathbf{K}}_{\text{GM}}^e + \bar{\mathbf{K}}_{\text{GM2}}^e - \mathbf{K}_{\text{GAe}}^e. \end{aligned} \quad (83)$$

4. Numerical analysis

The beams considered in the analysis are made of four Carbon Fibre Reinforced Polymer (CFRP) material layers. Simply-supported boundary conditions are considered and piezoelectric patches are bonded to the external surfaces of the beams. Several configurations are chosen to assess the models for various geometrical properties and for a different actuator location and beam lamination, which is either cross-ply symmetric with a $[0^\circ/90^\circ/90^\circ/0^\circ]$ fibre orientation, or non-symmetric

Beam	L (mm)	b (mm)	h (mm)	Ply orientations
BPZT1	298.0	20.83	0.65	$[0^\circ/90^\circ/90^\circ/0^\circ]$
BPZT2	299.0	23.03	0.73	$[90^\circ/0^\circ/90^\circ/0^\circ]$
BPZT3	447.5	21.46	0.72	$[0^\circ/90^\circ/90^\circ/0^\circ]$
BPZT4	448.0	22.59	0.75	$[90^\circ/0^\circ/90^\circ/0^\circ]$
BPZT5	448.5	22.24	0.78	$[90^\circ/0^\circ/90^\circ/0^\circ]$

Table 1: Beam geometrical properties and material orientation.

with a $[90^\circ/0^\circ/90^\circ/0^\circ]$ fibre orientation. The names and geometrical properties of the beams are indicated in Table [1]¹. BPZT1 and BPZT2 have approximately the same length, but BPZT1 has a symmetric lamination and two actuators symmetrically located on the top and the bottom surface of the beam, whereas BPZT2 is slightly thicker and wider than BPZT1 and has a non-symmetric lamination with only one actuator bonded to the top surface. BPZT(3-5) have similar length and thickness values. BPZT3 and BPZT4 have one actuator on the top surface, whereas BPZT5 has two actuators bonded to the top and the bottom surface of the beam; BPZT3 has a symmetric lamination, BPZT4 and BPZT5 have both a non-symmetric lamination.

The beams are represented in Figs.[6], where the symmetric (S) and non-symmetric (NS) lamination is also indicated. The location of the actuators is expressed by the distance between the hinged edge of the beam and the first section of the patch, indicated as l_a or l_b in Figs.[6]. The midsection of the actuators in BPZT(1-2) is almost coincident to the central section of the corresponding beam (the eccentric distance is only 0.5 mm), whereas BPZT(3-4) have the actuator placed off the beam centre with an eccentric distance of 25.75 mm and 25.5 mm, respectively. The actuators of BPZT5 have the highest eccentric distance, 111.25 mm for the patch on the top and 111.75 mm for the patch at the bottom, being very close to the beam ends.

The beam BPZT1 has two actuators symmetrically located with respect to the mid-plane, one on the top and one on the bottom surface of the beam, whereas BPZT5 has the two actuators in different locations along the beam length (indicated as the distances l_a and l_b from the hinged edge in Fig.[6e]).

Each actuator patch has two external parts made of Kapton (Young modulus of 2,500 MPa and Poisson ratio of 0.34 [40]) of length $l_k = 8$ mm each, and an internal area made of piezoelectric material with a length $l_p = 85$ mm (see Fig.[7]). The thickness is $h_p = 0.3$ mm and the width is assumed to be the same as the beam on which the patch is bonded. The dimensions and the material properties of the actuators correspond to the MFC 8514-P1 piezoelectric transducer [41]. MFC-P1 piezo-composite actuators have superior actuation performances due to their complex structure made of piezoelectric rods and interdigitated electrodes. Their operational mode is called d_{33} -coupling and it slightly differs from the opera-

¹The beams considered in this study correspond to samples realised for experimental tests.

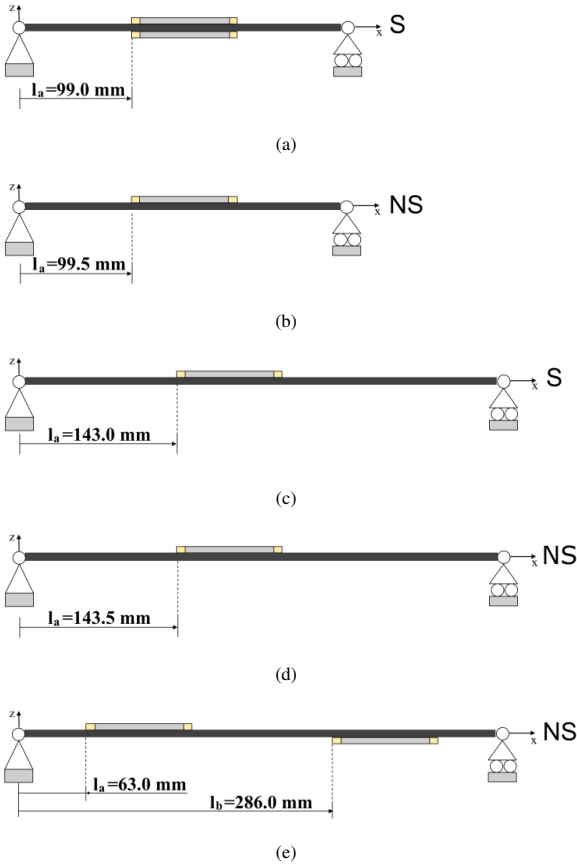


Figure 6: Composite beams with piezoelectric actuators patches: (a) beam BPZT1, (b) beam BPZT2 (c) beam BPZT3 (d) beam BPZT4 (e) beam BPZT5.

tional mode considered in the new RZT formulation, called d_{31} -coupling. The detailed model of the MFC transducers is not a purpose of the present work, thus a strategy to model their behaviour as a d_{31} -coupling is shown in Appendix D.

The properties of the CFRP used for the beams correspond to those of the carbon/epoxy unidirectional prepreps VTM264-T700 (35% of resin content, Advanced Composites Group). The characteristics of the VTM264-T700 and the piezoelectric properties of the actuator are reported in Table [2].

The presence of only one actuator or two actuators not symmetrically located on the top and bottom surfaces of BPZT(2-5) changes the location of the beam centroidal axis, thus the physical interfaces are characterised by both a change of material lamination and an offset of the half-thickness axis. Considering the coordinate reference system of Figs.[6], the offset is positive for $z > 0$ and it corresponds to $+h_p/2$ for the actuators of BPZT(2-4) and the first actuator of BPZT5, whereas it is $-h_p/2$ for the actuator bonded to the bottom surface of BPZT5.

4.1. RZT model

The finite element formulation based on the RZT for geometrically imperfect composite beams with piezoelectric actuators was implemented in a Matlab routine for linear-static, buckling and nonlinear static analyses. The number of finite elements in the RZT models was set taking into account the discontinuities

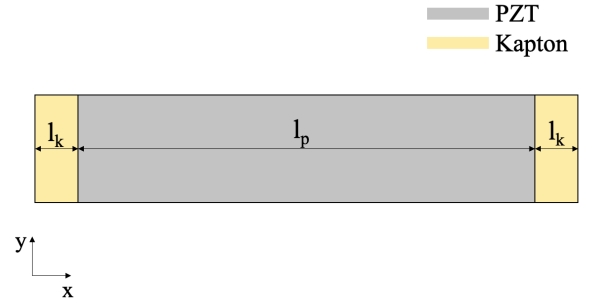


Figure 7: Model of the piezoelectric actuator patch.

CFRP		Piezoelectric [41]	
E_1 (MPa)	120,000	E_1 (MPa)	30,340
E_2 (MPa)	7,500	E_2 (MPa)	15,860
E_3 (MPa)	7,500	E_3 (MPa)	15,860
G_{12} (MPa)	3,900	G_{12} (MPa)	5,510
G_{13} (MPa)	3,900	G_{13} (MPa)	5,510
G_{23} (MPa)	2,300	G_{23} (MPa)	5,510
ν_{12}	0.32	ν_{12}	0.31
ν_{13}	0.32	ν_{13}	0.31
ν_{23}	0.20	ν_{23}	0.16
		d_{31} (m/V)	2.76×10^{-10}
		χ_{33} (F/m)	1.64×10^{-8}

Table 2: Mechanical properties of the materials of the beams and actuators.

along the beam length by considering a node at each physical interface. The two, closest and consecutive interfaces had the same distance for all the beams, corresponding to $l_k = 8$ mm. Indeed, one interface was between the part of the beam without the actuator and the part of the beam with a Kapton layer, and the other interface was between the part of the beam with a Kapton layer and the beam with the piezoelectric material. Any other pair of consecutive interfaces had a higher distance. For this reason, the maximum allowable length of the finite elements that could guarantee a uniform mesh was 8 mm. Buckling and postbuckling analyses were performed several times progressively reducing the element average length starting from 8 mm, thus increasing the number of finite elements. It was verified that the difference between the solutions obtained for a mesh with elements 2 mm long and the solutions with smaller elements was less than 0.01%, thus the average length of the finite elements considered in the RZT models was 2 mm. The resulting number of nodes and finite elements is indicated in Tables [3-4].

4.2. Abaqus model

The mesh of the Abaqus models used 3D stress elements for the actuators (C3D8/C3D8E type) and continuum shell elements for the beams (SC8R type). A number of two finite elements was set along the direction of the z -coordinate in order to have three nodes along the beam thickness. The average dimensions of the continuum shell elements were $1 \times 1 \times h$ mm³,

	No. of nodes			
	RZT	ABAQUS		
		Beam	Actuator	total
BPZT1	145	19,800	4,488	28,776
BPZT2	145	21,672	4,896	26,568
BPZT3	223	29,634	4,488	34,122
BPZT4	225	32,400	4,896	37,296
BPZT5	219	31,050	4,692	40,434

Table 3: Number of nodes of the RZT and the Abaqus models.

	No. of elements			
	RZT	ABAQUS		
		Beam	Actuator	total
BPZT1	144	12,558	2,121	16,800
BPZT2	144	13,800	2,323	16,123
BPZT3	222	18,816	2,121	20,937
BPZT4	224	20,654	2,323	22,977
BPZT5	218	19,756	2,222	24,200

Table 4: Number of finite elements of the RZT and the Abaqus models.

where h was half the thickness of the beam considered. As shown in Fig.[8], only one element was considered along the actuator thickness direction, thus the average dimensions of the 3D stress elements were $1 \times 1 \times h_p \text{ mm}^3$. Tables [3-4] report the number of nodes and finite elements also for the Abaqus models, distinguishing the values for the beam part and for each actuator.

A tie constraint was used to connect the patch to the beam surfaces. Simply-supported boundary conditions were defined at the half-thickness nodes of the beam edges and concentrated compression forces were applied to all the nodes at the supported edge.

5. Results

In this section, the analyses performed for both the RZT and the Abaqus finite element models are presented. In each case, the results of RZT were compared to the Abaqus solutions to evaluate the differences between RZT and highly detailed finite element models in commercial codes.

Firstly, buckling analyses were conducted to verify the RZT abilities of predicting the critical buckling loads of composite beams with physical discontinuities. Subsequently, nonlinear static analyses were performed to assess the accuracy of RZT with respect to Abaqus also for the evaluation of the post-buckling behaviour of composite beams with actuator patches bonded to the external surfaces. Finally, the ability of the new

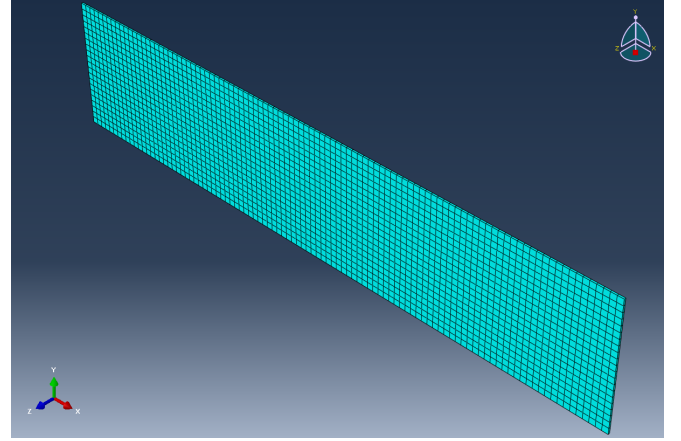


Figure 8: Abaqus finite element model of the piezoelectric actuator using 3D elements.

RZT formulation, that includes the inverse piezoelectric behaviour, was assessed by performing nonlinear static response analyses to a piezoelectric voltage in the actuators.

5.1. Buckling analysis

The RZT buckling loads were calculated solving the eigenvalue problem of Eq.[53] with $P_i^e = -N_{xc}^e = N_0$ and $N_x^{inde} = 0$ because the piezoelectric actuators were imagined to be disconnected from any power supply. The degrees of freedom vector and the stiffness matrices had to be modified as shown in Eq.[64] because the presence of piezoelectric patches bonded to the external surfaces of the beams introduced 4 geometrical interfaces for BPZT(1-4) and 8 geometrical interfaces for BPZT5. In Abaqus, axial-compressive forces of the same intensity were applied to the nodes at the supported edge with a total applied load $N_0 = 1 \text{ N}$ (see Fig.[9]), thus the eigenvalues obtained from a buckle-perturbation analysis corresponded to the actual buckling loads.

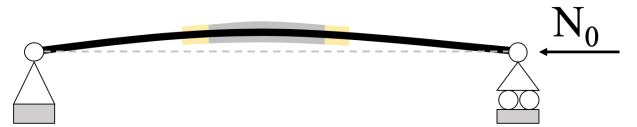


Figure 9: BPZT1 subjected to a compressive load N_0 .

Table [5] shows the first two buckling loads calculated with Abaqus and RZT and the percentage deviation, Δ , of RZT with respect to Abaqus. All the values of Δ were less than 3%, and Δ exceeded 2% only for BPZT5. The BPZT5 beam had the highest level of non-symmetry due to a non-symmetric beam lamination and location of the actuators, and likely this was the reason of the highest deviation between the two solutions.

The time required to perform the buckling analyses using the Matlab routine based on RZT and Abaqus is reported in Table [6]. It can be seen that the time of the Abaqus analyses increases with the number of finite elements, whereas the RZT computational cost is significantly affected by the non-symmetry of the

	ABAQUS (N)	RZT (N)	Δ %
BPZT1	8.56	8.40	-1.88
	24.61	24.40	-0.86
BPZT2	6.00	5.90	-1.71
	19.08	18.90	-0.92
BPZT3	4.07	4.00	-1.65
	14.57	14.47	-0.67
BPZT4	2.56	2.52	-1.41
	8.97	8.90	-0.80
BPZT5	2.92	2.85	-2.62
	14.46	14.07	-2.67

Table 5: Buckling loads of composite beams with piezoelectric actuators.

	RZT	ABAQUS
BPZT1	1.9	13.5
BPZT2	7.5	11.8
BPZT3	1.8	14.4
BPZT4	7.3	16.0
BPZT5	7.8	17.6

Table 6: Time (s) required by RZT and Abaqus for performing the buckling analysis.

lamination rather than by the number of finite elements considered in the model. As an example, the RZT finite element model of BPZT3 has 78 elements more than BPZT1 (refer to Table [4]), but the time to perform the buckling analysis is almost the same for both beams. By contrast, the time to perform the buckling analysis with RZT for BPZT2 is four times the time required for BPZT1, even if the two beams have the same number of finite elements. The comparison between RZT and Abaqus in Tables [5-6] shows that the models based on one-dimensional RZT finite elements are not only as accurate as the three-dimensional Abaqus models for predicting the critical buckling load, but they are also convenient in terms of computational time because Abaqus requires double the RZT time for the buckling analysis of almost all the beams with a non-symmetric lamination and six times the RZT time for symmetrically laminated beams.

5.2. Static nonlinear response to a compressive load

The postbuckling behaviour of the beams was studied by progressively increasing the applied compressive load N_0 from 0 N to a value corresponding to 99% the critical buckling load, N_{cr} . For the RZT models, the response was calculated by solving Eq.[66] using the Newton-Raphson method with increments on the mechanical load (refer to Eqs.[67, 70-73]).

In addition, the internal axial force of a beam in simply-supported boundary conditions with an applied compressive load, as the one shown in Fig.[9], is independent of the degrees of freedom, thus the beam response was calculated also using

	BPZT1	BPZT2	BPZT3	BPZT4	BPZT5
a₁	1.66	3.97	1.60	8.62	9.24
a₂	0.10	0.19	0.76	-0.15	-0.36
a₃	0.27	0.30	0.22	0.72	0.46

Table 7: Coefficients of the linear combination approximating the imperfection function.

the simplified equilibrium equation for beams with a constant internal axial force, whose element-based formulation corresponds to Eq.[52]. The piezoelectric actuators were imagined to be disconnected from any power supply, thus $N_x^{inde} = 0$ and $N_{xc}^e = -N_0$ for all the finite elements of the model.

All the vectors and matrices in the equilibrium equations had to be formulated according to the procedure shown in Section 3.3 to take into account the physical interfaces due to the presence of the actuators.

The geometric imperfections of the beams were considered in terms of an initial stress-free deflection from a straight axis configuration, introducing them in the finite element models as a linear combination of the buckling modes of the beams without imperfections. In the RZT models, the imperfection was described by the function $w^*(x)$, defined as a linear combination of the first three buckling mode functions of a simply supported beam:

$$w^*(x) = a_1 \cdot \sin\left(\frac{\pi x}{L}\right) + a_2 \cdot \sin\left(\frac{2\pi x}{L}\right) + a_3 \cdot \sin\left(\frac{3\pi x}{L}\right). \quad (84)$$

The coefficients a_k ($k = 1, 2, 3$) of the linear combination were different for each beam, as indicated in Table [7]². The same coefficients were used in Abaqus to define the imperfection as a linear combination of the buckling modes of the Abaqus buckling analyses. However, the use of the same coefficients for both the RZT and the Abaqus models led to slightly differently imperfect beams, because the initial stress-free deformed shapes of the Abaqus beams were obtained combining buckling modes of three-dimensional models, whereas, in RZT, the buckling mode shapes were those of one-dimensional models.

The Riks analysis [42] was implemented in Abaqus with an initial increment of 0.01, a maximum increment of 0.1 and a maximum number of increments corresponding to 1000. In RZT, the same maximum and minimum values of increments were considered. The solution of Eq.[52] was calculated for 40 values of N_0 , obtained by constant load increments from 0 N to 99% of the critical buckling load.

The load-displacement equilibrium paths obtained performing the nonlinear static analysis are shown in Figs.[10-14] for the RZT and the Abaqus models. The three solutions identified the exact same initial responses in the range of loads where the

²The finite element models of this study correspond to beams realised for experimental tests. The values a_k considered for defining the function $w^*(x)$ are those that approximate the actual initial deflection measured on the real beams.

relationship between N_0 and the transversal displacement was linear. In general, a very good agreement between the Abaqus and the RZT- N_0 solutions was found for any value of N_0 , also for non-symmetric laminations. As a general behaviour, the RZT solution obtained by solving Eq.[66], which was indicated as RZT-nnl, was stiffer than Abaqus in any case according to the lower number of degrees of freedom of the models. On the other hand, the simplified RZT solution obtained from Eq.[52] was slightly softer than Abaqus.

The best results in terms of lowest deviation of both the RZT solutions from Abaqus were obtained for BPZT1 and BPZT3 in Figs.[10,12], which were the beams with a symmetric lamination. Moreover, even if BPZT3 had only one piezoelectric patch bonded to the top external surface, which made the lamination globally non-symmetric in a small portion of the beam, the RZT-nnl and the Abaqus curves were very close for any applied compressive load value. The deviation of the RZT-nnl solution from Abaqus did not exceed 10% even at the highest values of N_0 , reaching 9.49% for BPZT1 and 6.1% for BPZT3. In addition, the deviation of the RZT- N_0 from Abaqus had further lower values reaching, respectively, -1.05% and -1.19% at the highest value of applied compressive load.

A bigger mismatch between RZT-nnl and Abaqus was found for BPZT2, BPZT4 and BPZT5 at high values of N_0 in Figs.[11,13-14], where the deviation exceeded 20% in all cases. These beams had a non-symmetric lamination and actuator patches located unsymmetrically along the beam length. In addition, for these beams there was also a higher difference between the initial geometric imperfection of the RZT and the Abaqus models, which reached 0.9% and 2% for BPZT(2,4) and BPZT5 respectively, whereas it was only 0.1% for BPZT(1,3).

Despite these slight differences between the RZT-nnl and the Abaqus results, the RZT- N_0 solutions were remarkably close to the Abaqus predictions with a deviation always lower than 2.5%, even for highly non-symmetric beams.

Table [9] shows that both the RZT procedures have a considerably lower computational cost than the Abaqus analyses for all the beams. This was the application where the RZT capabilities were best shown because, even for very slender beams and simple geometries, the time for performing nonlinear Riks analyses in Abaqus was significantly high, exceeding 10 minutes for all cases, whereas RZT-nnl was less than 5 minutes on average and RZT- N_0 was even less than 60 s, being also as accurate as Abaqus.

	RZT		ABAQUS
	nnl	N_0	
BPZT1	310	38	1264
BPZT2	166	56	638
BPZT3	227	38	637
BPZT4	244	56	704
BPZT5	209	58	1887

Table 8: Time (s) required by RZT and Abaqus for performing the nonlinear analysis.

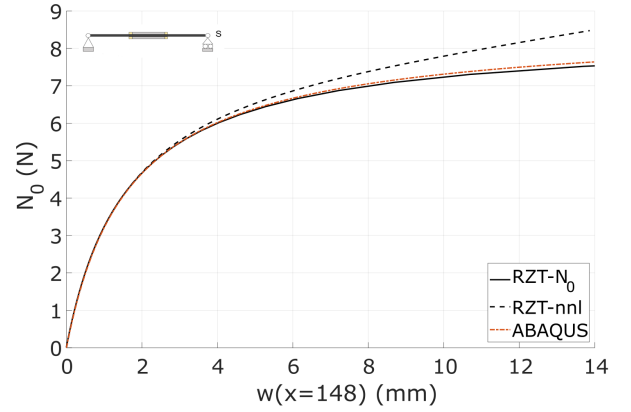


Figure 10: Load-displacement equilibrium path of BPZT1.

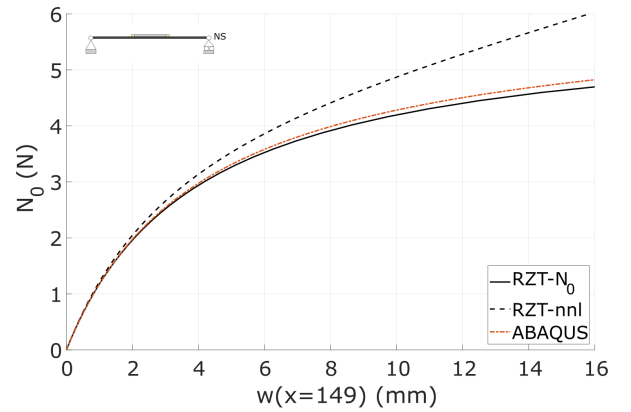


Figure 11: Load-displacement equilibrium path of BPZT2.

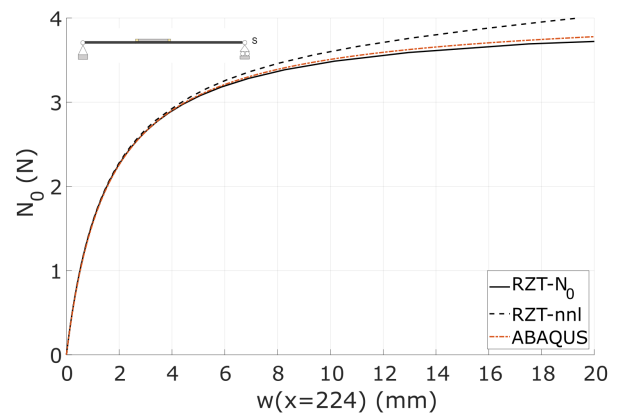


Figure 12: Load-displacement equilibrium path of BPZT3.

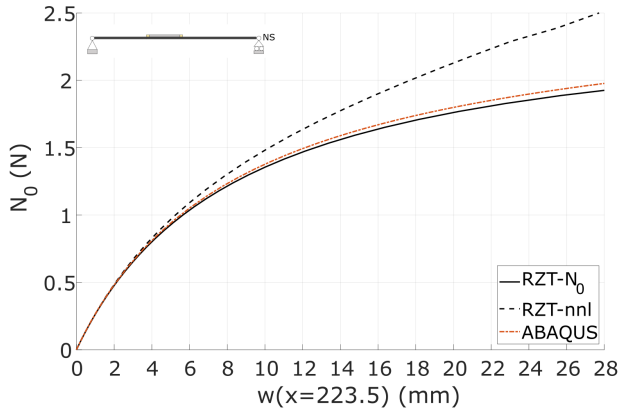


Figure 13: Load-displacement equilibrium path of BPZT4.

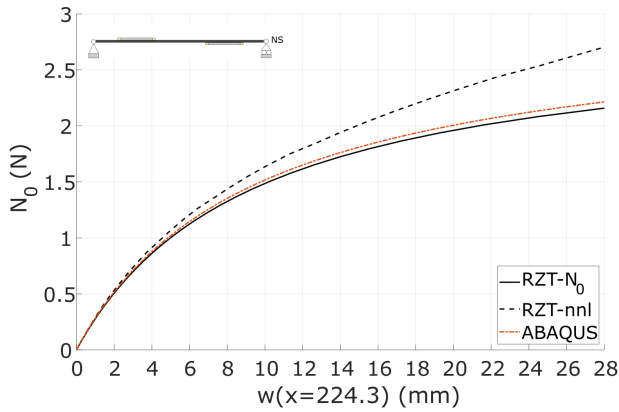


Figure 14: Load-displacement equilibrium path of BPZT5.

5.3. Voltage response

The transversal deflection of the beams was calculated considering a voltage source connected to the piezoelectric patches. The e_{31} operational mode was considered for the actuators in both the RZT-nnl and the Abaqus models, with a piezoelectric stress coefficient $e_{31} = 0.0084 \text{ N}/(\text{mm}\cdot\text{V})$. The constraining conditions assumed for this application were two hinges at the beam ends and the voltage applied to the actuators was the only external action considered on the beams. In these loading and boundary conditions, the RZT response of the beams could be calculated by solving Eq.[66] with the Newton-Raphson method incrementing the electric voltage and considering $\mathbf{F} = 0$ (refer to Eqs.[67-69] and Eqs.[72-73]). Firstly, the beams were deflected in the opposite direction of the imperfection by applying a negative voltage to all the actuators but the one on the bottom surface of the BPZT1, which had positive values instead (see Fig.[15a]). Then, the RZT results were verified also for positive transversal deflections obtained by applying values of voltage opposite to the previous case, as shown in Fig.[15b]. The range of voltage values considered varied between 0 V and $\pm 700 \text{ V}$.

The piezoelectric behaviour was introduced in Abaqus by modelling the piezoelectric part of the actuators with C3D8E finite elements. The voltage was defined as a boundary condition

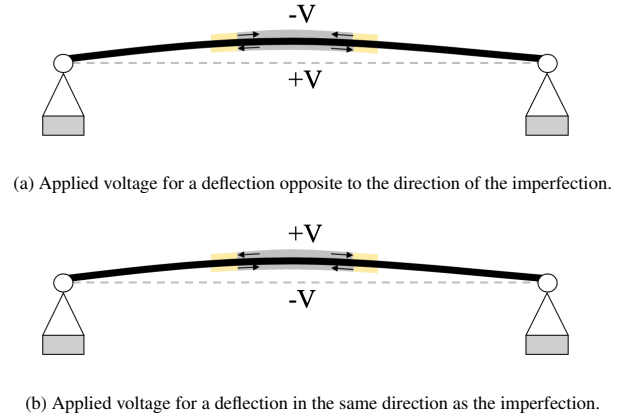


Figure 15: Actuation modes for BPZT1.

applied to the top and bottom surfaces of the actuator. According to the positive value of e_{31} , the actuator had to expand when the electric field deriving from the voltage difference between the top and bottom surface was positive, i.e. the electric field vector had the same orientation as the z -axis.

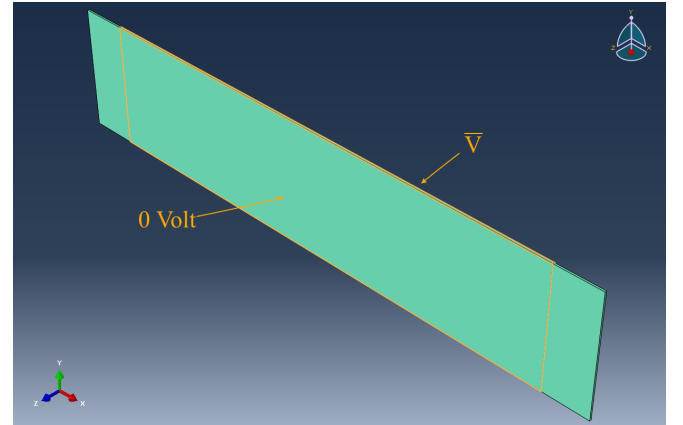


Figure 16: Modelling piezoelectric actuators in Abaqus with a e_{31} operational mode.

For this reason, a voltage of 0 V was applied to the top surface (with respect to the z -axis) and a voltage \bar{V} was applied to the bottom surface of each actuator, as shown in Fig.[16]. As a consequence, positive values of \bar{V} caused the expansion of the actuators, whereas negative values of \bar{V} caused a contraction.

In Abaqus, a general nonlinear static analysis was performed for the beams with the geometric imperfections defined as a linear combination of the buckling modes, as described in the previous section.

The transversal deflection of the beams as a function of the increasing absolute value of voltage is reported in Figs.[17-21] for both the RZT and the Abaqus models, referring to the same points along the x -direction considered in the previous analysis. The solutions obtained for voltages which deflected the beam opposite to its initial imperfections, indicated as RZT- and Abaqus-, and the solutions which gave positive transversal deflections, indicated as RZT+ and Abaqus+, were reported in

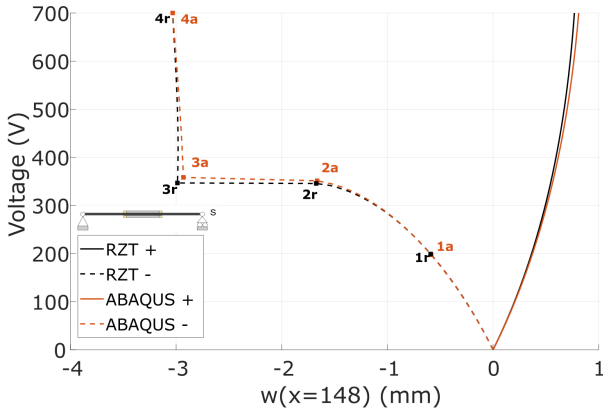


Figure 17: BPZT1 response for increasing voltage values.

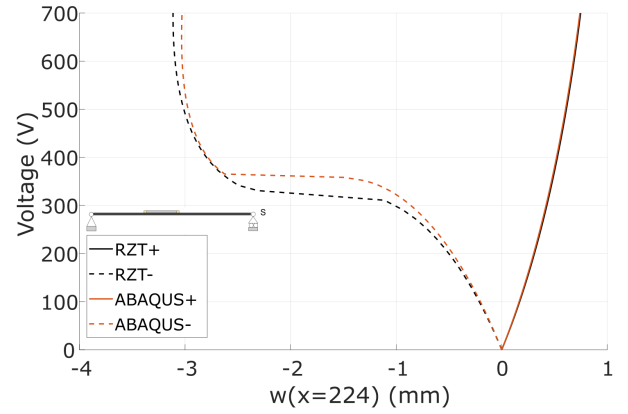


Figure 19: BPZT3 response for increasing voltage values.

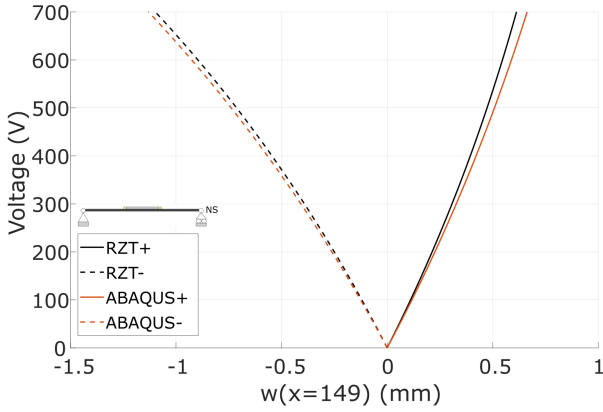


Figure 18: BPZT2 response for increasing voltage values.

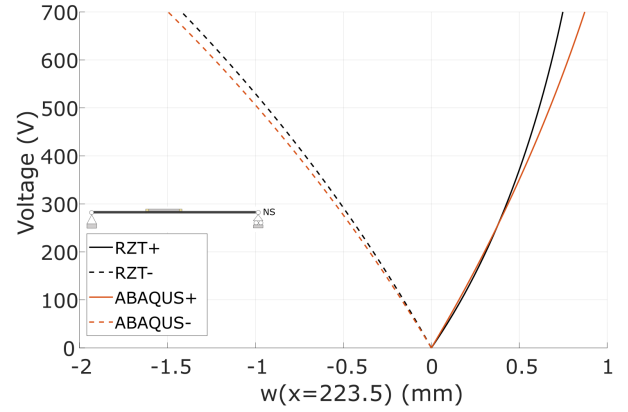


Figure 20: BPZT4 response for increasing voltage values.

the same figure for each beam.

The comparison between the Abaqus and the RZT solutions indicates that RZT was extremely accurate, even for very high voltage values, for both the cases of positive and negative transversal displacements.

RZT correctly predicted the curvature change in the response of the BPZT1 and the BPZT3 (Figs.[17]-[19]), which took place when the transversal displacement w reached exactly the opposite value of the beam initial deviation in that point. Further increasing the voltage, the beam started to bend in the opposite direction, and the curvature changed. RZT predicts this behaviour with a remarkable accuracy, especially for BPZT1 and the very good agreement with the Abaqus solution is for the deflection of all the points along the beam axis. Fig.[22] reports the deformed shape of BPZT1 for different applied voltage values. The curves indicated as 0r and 0a correspond to the initial stress-free deflections of the RZT beam and the centroidal axis of the Abaqus beam, respectively. The remaining curves are the deformed shapes of the RZT and the Abaqus models for the voltage values highlighted in Fig.[17]. The 1r and 1a solutions are obtained for an applied voltage of 200 V, whereas 2(r-a) and 3(r-a) are the solutions obtained for the voltage values before and after the snapping through of the beam. Note that in Fig.[22] the transversal displacement values, w , given by the in-

tersection of $x=148$ mm and each deformed shape correspond to those of the points indicated in Fig.[17] for the voltage values considered. The results of Fig.[22] show the high accuracy of RZT in predicting the deformed shapes for varying voltage, before and after the snap through, and also the value of voltage at which the snap through took place, which was around 350 V.

The other beams did not exhibit this behaviour in the range of voltage considered because their initial imperfection was too large, thus higher voltages were needed to invert the deflection. The biggest difference between the two solutions was found for BPZT4 in Fig.[20] at high values of positive \bar{V} , where the RZT was slightly stiffer than Abaqus, and for BPZT5 in Fig.[21] at high values of negative \bar{V} , where RZT was softer instead. This behaviour was likely a consequence of the fact that the initial imperfections of the RZT and the Abaqus models were not exactly the same and these beams had the highest mismatch, as discussed above. Fig.[21] also shows that even the application of a positive voltage higher than 250 V causes a deflection of the point at half-length of the beam towards the negative values of the z -axis.

The time to perform the analysis with RZT and in Abaqus is reported in Table [9], which indicates that RZT is computationally more efficient than the Abaqus model also in this case performing the same analysis in half the time. Moreover, the

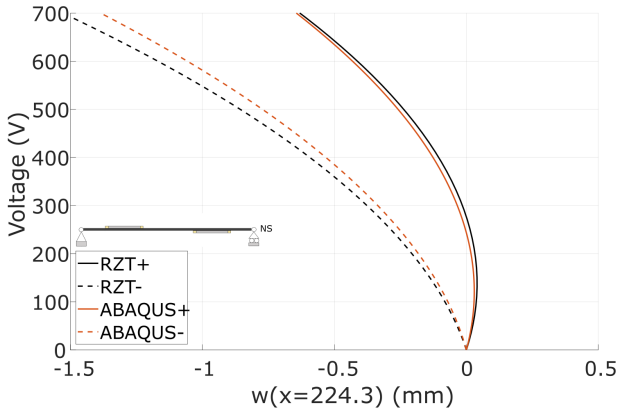


Figure 21: BPZT5 response for increasing voltage values.

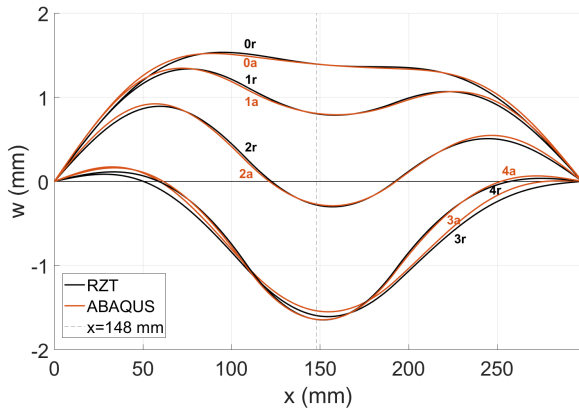


Figure 22: Deformed shapes of BPZT1 for different values of applied voltage.

Abaqus values in Table [9] are those obtained for a general nonlinear static analysis, which is generally faster than the Riks analysis; this means that the investigation of the postbuckling behaviour of beams with active piezoelectric actuators would require a higher computational cost.

	Actuation Response	
	RZT	ABAQUS
BPZT1	145	420
BPZT2	138	300
BPZT3	226	402
BPZT4	216	403
BPZT5	211	570

Table 9: Time (s) required by RZT and Abaqus for performing the nonlinear static analysis of the beams subjected to the piezoelectric voltage.

6. Conclusion

A new formulation of the Refined Zigzag Theory for evaluating the nonlinear static response, the buckling loads and the postbuckling behaviour of initially imperfect composite beams

with piezoelectric actuators was presented and numerically verified. The nonlinear formulation of RZT for initially imperfect beams was extended to include piezoelectric actuator layers in the analytical model and the procedure to derive the nonlinear equilibrium equations employing the Principle of Virtual Work for electro-mechanical systems was described in detail. A finite element approximation based on C^0 RZT-beam finite elements was created, providing a method to solve the equilibrium problem for any lamination, load system, boundary conditions and geometric imperfection. Moreover, the method was further generalised to the case of piezoelectric actuator patches by introducing a strategy based on the Lagrange multipliers able to model the geometric discontinuities (variation of thickness and material lamination) due to actuator patches bonded on the external surface of the beam. The general form of the resulting FE equilibrium equation was nonlinear and had both mechanical and electrical load terms. The incremental-iterative technique based on the Newton-Raphson method was proposed as the procedure to solve the FE nonlinear equilibrium equation and the formulations to solve both cases of incremental electrical forces and incremental mechanical forces were shown. The model was employed for the analysis of five CFRP beams with actuator patches bonded to the beam external surfaces in different locations, assessing the model validity for different geometrical properties of the beams and for symmetric and non-symmetric material laminations. Highly-detailed finite element models of the beams were developed in Abaqus employing three-dimensional finite elements. The new RZT-FE formulation was compared to the Abaqus solutions for three different analyses: the critical buckling load, the static nonlinear response to a compressive load and the nonlinear static response of the beam to a voltage applied to the actuators. The RZT model was extremely accurate for calculating the critical buckling loads with a percentage deviation with respect to the Abaqus solution higher than 2% only for one beam, where it reached 2.7%. The RZT prediction of the beam postbuckling behaviour was very accurate as well. In this analysis, the solution of the RZT model obtained with the Newton-Raphson method was a bit stiffer than Abaqus for values of applied compressive loads close to the critical buckling load. However, the solutions obtained employing the RZT simplified equilibrium equation for beams with a constant axial force were very close to Abaqus for any applied compressive load, with a deviation lower than 2.5% in any case. Moreover, the new nonlinear RZT model successfully predicted also the nonlinear response of the beams to increasing voltage values applied to the actuators, even for highly nonlinear behaviours. The great advantages of the proposed RZT model were demonstrated by comparing the computational time required to perform the analyses. In any case, the RZT model required significantly less time than Abaqus, especially in the postbuckling analysis where Abaqus exceeded 10 minutes whereas the simplified formulation of RZT required less than 60 s.

Acknowledgements

The authors acknowledge the RMIT University for supporting this work through the HDR Post-submission Grant.

References

- [1] Wilkie WK, Inman DJ, High JW, Williams RB, Recent developments in NASA piezocomposite actuator technology, Tech. Rep. 20040082248, NASA (2004).
- [2] Bent AA, Active fiber composite material systems for structural control applications, in: *Smart Structures and Materials 1999: Industrial and Commercial Applications of Smart Structures Technologies*, Vol. 3674, International Society for Optics and Photonics, 1999, pp. 166–177.
- [3] Lin XJ, Zhou KC, Zhang XY, Zhang D, Development, modeling and application of piezoelectric fiber composites, *Trans Nonferrous Met Soc China* 23 (1) (2013) 98–107.
- [4] Wilkie WK, Bryant RG, High JW, Fox RL, Hellbaum RF, Jalink Jr A, Little BD, Mirick PH, Low-cost piezocomposite actuator for structural control applications, in: *Smart structures and materials 2000: industrial and commercial applications of smart structures technologies*, Vol. 3991, International Society for Optics and Photonics, 2000, pp. 323–334.
- [5] Wlezien R, Horner G, McGowan A, Padula S, Scott M, Silcox R, Simpson J, The aircraft morphing program, in: *39th AIAA/ASME/ASCE/AHS/ASC Structures, Structural Dynamics, and Materials Conference and Exhibit*, 1998, pp. 1–13.
- [6] Ho Duc D, Mura R, Piroddi L, Lovera M, Ghiringhelli GL, Robust harmonic control: an application to structural vibration reduction in helicopters, *IFAC-PapersOnLine* 48 (9) (2015) 263–268.
- [7] Lee YY, Lam KC, Yuen KK, Lam HF, Yao J, Active vibration control of an aircraft cabin panel using piezoelectric sensors and actuators, *Int J Struct Stab Dyn* 3 (1) (2003) 131–141.
- [8] Hu Q, Ma G, Variable structure control and active vibration suppression of flexible spacecraft during attitude maneuver, *Aerosp Sci Technol* 9 (4) (2005) 307–317.
- [9] Zhang Z, Li Y, Yu X, Li X, Wu H, Wu H, Jiang S, Chai G, Bistable morphing composite structures: A review, *Thin-Walled Struct* 142 (2019) 74–97.
- [10] Aimmanee S, Tichakorn K, Piezoelectrically induced snap-through buckling in a buckled beam bonded with a segmented actuator, *J Intell Mater Syst Struct* 29 (9) (2018) 1862–1874.
- [11] Varelis D, Saravanos DA, Coupled nonlinear mechanics for the electromechanical response of multi-stable piezoelectric shallow shells with piezoelectric films, *Aerosp Sci Technol* 109 (2021) 106444.
- [12] de Faria AR, de Almeida SFM, Enhancement of pre-buckling behavior of composite beams with geometric imperfections using piezoelectric actuators, *Compos B Eng* 30 (1) (1999) 43–50.
- [13] Abramovich H, A new insight on vibrations and buckling of a cantilevered beam under a constant piezoelectric actuation, *Compos Struct* 93 (2) (2011) 1054–1057.
- [14] Kusagur SM, Arunkumar G, Manjunath TC, Use of smart intelligent sensor & actuator mechanical materials (pvdf/pzt) in developing mimo mathematical model of the smart structure and its use to control the active vibrations using discrete sliding mode control theory with output samples, *Mater Today* 37 (2021) 1592–1602.
- [15] Moory-Shirbani M, Sedighi HM, Ouakad HM, Najar F, Experimental and mathematical analysis of a piezoelectrically actuated multilayered imperfect microbeam subjected to applied electric potential, *Compos Struct* 184 (2018) 950–960.
- [16] Chen N, Yan P, Ouyang J, A generalized approach on bending and stress analysis of beams with piezoelectric material bonded, *Sens Actuators, A* 290 (2019) 54–61.
- [17] Abramovich H, Deflection control of laminated composite beams with piezoceramic layers—closed form solutions, *Compos Struct* 43 (3) (1998) 217–231.
- [18] Fridman Y, Abramovich H, Enhanced structural behavior of flexible laminated composite beams, *Compos Struct* 82 (1) (2008) 140–154.
- [19] Kusagur SM, Arunkumar G, Manjunath TC, Development of mathematical model for smart intelligent flexible structures using smart intelligent sensor & actuator materials using timoshenko beam theory & its control using pof, *Mater Today* 37 (2021) 648–655.
- [20] Mareishi S, Rafiee M, He XQ, Liew KM, Nonlinear free vibration, post-buckling and nonlinear static deflection of piezoelectric fiber-reinforced laminated composite beams, *Compos B Eng* 59 (2014) 123–132.
- [21] Tessler A, Di Sciuva M, Gherlone M, A refined zigzag beam theory for composite and sandwich beams, *J Compos Mater* 43 (2009) 1051–1081.
- [22] Gherlone M, On the use of zigzag functions in equivalent single layer theories for laminated composite and sandwich beams: a comparative study and some observations on external weak layers, *J Appl Mech* 80 (6) (2013) 061004.
- [23] Shen HS, Chen X, Huang XL, Nonlinear bending and thermal postbuckling of functionally graded fiber reinforced composite laminated beams with piezoelectric fiber reinforced composite actuators, *Compos B Eng* 90 (2016) 326–335.
- [24] Moradi-Dastjerdi R, Behdinan K, Safaei B, Qin Z, Buckling behavior of porous cnt-reinforced plates integrated between active piezoelectric layers, *Eng Struct* 222 (2020) 111141.
- [25] Komarsofla MK, Salami SJ, Shakeri M, Komarsofla AK, Active yielding control for coupled electro-mechanical bending response of piezoelectric functionally graded cylindrical panel based on full layer-wise theory, *Thin-Walled Struct* 154 (2020) 106848.
- [26] Robbins DH, Reddy JN, Analysis of piezoelectrically actuated beams using a layer-wise displacement theory, *Comput Struct* 41 (2) (1991) 265–279.
- [27] Tahani M, Analysis of laminated composite beams using layerwise displacement theories, *Compos Struct* 79 (4) (2007) 535–547.
- [28] Hao YX, Zhao KF, Zhang W, Yang SW, Nonlinear dynamics and dynamic instability of smart structural cross-ply laminated cantilever plates with mfc layer using zigzag theory, *Appl Math Model* 79 (2020) 639–671.
- [29] Abaqus theory manual - beam element overview (2009). URL <https://classes.engineering.wustl.edu/2009/spring/mase5513/abaqus/docs/v6.5/books/stm/default.htm?startat=ch03s05ath73.html>
- [30] Ascione A, Gherlone M, Nonlinear static response analysis of sandwich beams using the refined zigzag theory, *J Sandw Struct Mater* 22 (7) (2020) 2250–2286.
- [31] Iurlaro L, Gherlone M, Mattone M, Di Sciuva M, Experimental assessment of the refined zigzag theory for the static bending analysis of sandwich beams, *J Sandw Struct Mater* 20 (2018) 86–105.
- [32] Iurlaro L, Ascione A, Gherlone M, Mattone M, Di Sciuva M, Free vibration analysis of sandwich beams using the refined zigzag theory: an experimental assessment, *Meccanica* 50 (2015) 2525–2535.
- [33] Ascione A, Orifici AC, Gherlone M, Experimental and numerical investigation of the refined zigzag theory for accurate buckling analysis of highly heterogeneous sandwich beams, *Int J Struct Stab Dyn* 20 (07) (2020) 2050078.
- [34] Ghorbanpour Arani A, Mosayyebi M, Kolahdouzan F, Kolahchi R, Jamali M, Refined zigzag theory for vibration analysis of viscoelastic functionally graded carbon nanotube reinforced composite microplates integrated with piezoelectric layers, *Proc Inst Mech Eng, Part G* 231 (13) (2017) 2464–2478.
- [35] Gherlone M, Tessler A, Di Sciuva M, C^0 beam elements based on the refined zigzag theory for multilayered composite and sandwich laminates, *Compos Struct* 93 (2011) 2882–2894.
- [36] Brockmann TH, *Theory of Adaptive Fiber Composites*, Springer, 2009.
- [37] Brush DO, Almroth BO, *Buckling of bars, plates and shells*, McGraw-Hill, 1975.
- [38] Fasano FC, Sviluppo e implementazione di tecniche di interfaccia per elementi finiti trave, Master's thesis, Politecnico di Torino (2008).
- [39] Crisfield MA, *Non-linear Finite Element Analysis of Solids and Structures*, John Wiley & Sons, 1991.
- [40] Chiarelli MR, Binante V, Botturi S, Massai A, Kunzmann J, Colbataldo A, Romano DG, On the active deformations of hybrid specimens, *Aircr Eng Aerosp Technol* 88 (5) (2016) 676–687.
- [41] Smart Material, Macro fiber composite data sheet (2000–2017).
- [42] Dassault Systemes Simulia Corporation, *Abaqus Analysis User's Manual*, 6.8 Edition (2008).

Appendix A. Vectors and matrices definitions

The matrices appearing in Eq.[6] are:

$$\mathbf{Z}_\epsilon^{(k)} = \begin{bmatrix} 1 & 0 & 0 & 0 & z & \phi^{(k)} \end{bmatrix}, \quad (\text{A.1})$$

$$\mathbf{Z}_\gamma^{(k)} = \begin{bmatrix} 0 & 1 & 1 & \beta^{(k)} & 0 & 0 \end{bmatrix}, \quad (\text{A.2})$$

and

$$\mathbf{H} = \begin{bmatrix} 0 & 0 & 0 & 0 & 0 & 0 \\ 0 & 1 & 0 & 0 & 0 & 0 \\ 0 & 0 & 0 & 0 & 0 & 0 \\ 0 & 0 & 0 & 0 & 0 & 0 \\ 0 & 0 & 0 & 0 & 0 & 0 \\ 0 & 0 & 0 & 0 & 0 & 0 \end{bmatrix}. \quad (\text{A.3})$$

The matrix of the stiffness coefficient, Δ , in Eq.[18] is defined as

$$\Delta = \begin{bmatrix} A_{11} & 0 & 0 & 0 & B_{12} & B_{13} \\ 0 & \bar{G}A & \bar{G}A & (G - \bar{G})A & 0 & 0 \\ 0 & (G - \bar{G})A & (G - \bar{G})A & (\bar{G} - G)A & 0 & 0 \\ B_{12} & 0 & 0 & 0 & D_{11} & D_{12} \\ B_{13} & 0 & 0 & 0 & D_{12} & D_{22} \end{bmatrix}, \quad (\text{A.4})$$

where the stiffness coefficients are

$$\begin{aligned} [A_{11}, B_{12}, D_{11}] &\equiv \int_A E_x^{(k)} [1, z, z^2] dA, \\ [B_{13}, D_{12}, D_{22}] &\equiv \int_A E_x^{(k)} \phi^{(k)} [1, z, \phi^{(k)}] dA, \end{aligned} \quad (\text{A.5})$$

and

$$\bar{G} \equiv \frac{1}{2h} \int_{-h}^{+h} G_{xz}^{(k)} dz, \quad (\text{A.6})$$

is the average thickness-weighted transverse-shear modulus of the total laminate. The vector $\bar{\Delta}$ in Eq.[18] corresponds to the first column of the matrix Δ .

The shape function matrix introduced for the finite element approximation in Eq.[26]

$$\mathbf{N} \equiv \begin{bmatrix} N_1^L & 0 & 0 & 0 & N_2^L & 0 & 0 & 0 \\ 0 & N_1^L & -l^e N_m^Q & -l^e r N_m^Q & 0 & N_2^L & l^e N_m^Q & l^e r N_m^Q \\ 0 & 0 & N_1^L & 0 & 0 & 0 & N_2^L & 0 \\ 0 & 0 & 0 & N_1^L & 0 & 0 & 0 & N_2^L \end{bmatrix}, \quad (\text{A.7})$$

where $l^e = L^e/8$, N_i^L are the linear Lagrange polynomials and N_j^Q are the quadratic Lagrange polynomials,

$$[N_1^L, N_2^L] = \left[\frac{1}{2}(1 - \xi), \frac{1}{2}(1 + \xi) \right], \quad (\text{A.8})$$

$$[N_1^Q, N_m^Q, N_2^Q] = \left[\frac{1}{2}\xi(\xi - 1), (1 - \xi^2), \frac{1}{2}\xi(\xi + 1) \right]. \quad (\text{A.9})$$

The matrix introduced in Eq.[28] containing the derivative of the shape functions is

$$\mathbf{B}^e \equiv \begin{bmatrix} N_{1,\xi}^L & 0 & 0 & 0 & N_{2,\xi}^L & 0 & 0 & 0 \\ 0 & N_{1,\xi}^L & -l^e N_{m,\xi}^Q & -l^e c N_{m,\xi}^Q & 0 & N_{2,\xi}^L & l^e N_{m,\xi}^Q & l^e c N_{m,\xi}^Q \\ 0 & 0 & L^e N_1^L & 0 & 0 & 0 & L^e N_2^L & 0 \\ 0 & 0 & 0 & L^e N_1^L & 0 & 0 & 0 & L^e N_2^L \\ 0 & 0 & N_{1,\xi}^L & 0 & 0 & 0 & N_{2,\xi}^L & 0 \\ 0 & 0 & 0 & N_{1,\xi}^L & 0 & 0 & 0 & N_{2,\xi}^L \end{bmatrix}. \quad (\text{A.10})$$

The finite element approximation of the initial imperfection function is obtained using the following shape function matrix:

$$\mathbf{N}^* \equiv [N_1^Q \quad N_m^Q \quad N_2^Q], \quad (\text{A.11})$$

and the matrix with the derivative of \mathbf{N}^* is

$$\omega^* \simeq \mathbf{B}^{*e} = \frac{1}{L^e} \begin{bmatrix} 0 & 0 & 0 \\ N_{1,\xi}^Q & N_{m,\xi}^Q & N_{2,\xi}^Q \\ 0 & 0 & 0 \\ 0 & 0 & 0 \\ 0 & 0 & 0 \end{bmatrix}. \quad (\text{A.12})$$

The matrices \mathbf{Z}_p^e and \mathbf{Z}_N^e introduced in Eq.[35] are

$$\mathbf{Z}_p^e \equiv \begin{bmatrix} a_E^1 & \dots & a_E^k & \dots & a_E^N \\ 0 & & 0 & & 0 \\ 0 & & 0 & & 0 \\ 0 & \dots & 0 & \dots & 0 \\ d_E^1 & & d_E^k & & d_E^N \\ c_E^1 & \dots & c_E^k & \dots & c_E^N \end{bmatrix}. \quad (\text{A.13})$$

$$\mathbf{Z}_N^e \equiv \int_A [E_x^{(k)} \mathbf{Z}_\epsilon^{(k)}] dA = \begin{bmatrix} A_{11}^e & 0 & 0 & 0 & B_{12}^e & B_{13}^e \end{bmatrix}, \quad (\text{A.14})$$

where A_{11}^e , B_{12}^e and B_{13}^e are the stiffness coefficients of the finite element e .

The matrix \mathbf{D} introduced in Eq.[36] is

$$\mathbf{D} \equiv \left[\int_A (\mathbf{Z}_\epsilon^{(k)T} E_x^{(k)} \mathbf{Z}_\epsilon^{(k)} + \mathbf{Z}_\gamma^{(k)T} G_{xz}^{(k)} \mathbf{Z}_\gamma^{(k)}) dA \right] \quad (\text{A.15})$$

Appendix B. Piezoelectric layer notations

The poling direction in each piezoelectric layer is parallel to the z -coordinates, as indicated in Fig.[B.23].

The top and the bottom surfaces have two different electric charges, q^- and q^+ , giving an electric potential difference $\Delta V^{(k)}$ parallel to the poling direction. For the assumptions made, the electric field vector, $\Xi^{(k)}$, and the electric displacement vector, $\mathbf{D}^{(k)}$, are

$$\Xi^{(k)} = \begin{Bmatrix} 0 \\ 0 \\ \Xi_z^{(k)} \end{Bmatrix}, \quad \mathbf{D}^{(k)} = \begin{Bmatrix} 0 \\ 0 \\ D_z^{(k)} \end{Bmatrix}. \quad (\text{B.1})$$

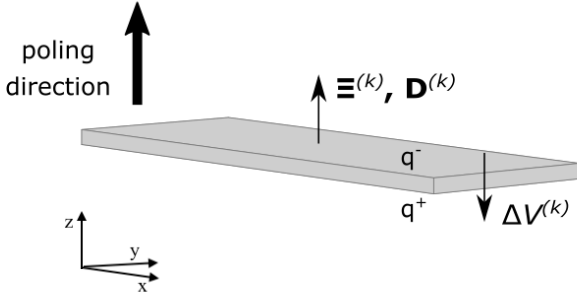


Figure B.23: Piezoelectric layers characteristics.

The electrostatic behaviour of the piezoelectric layers is assumed to be linear, thus the dielectric properties are not dependent on the electrostatic field intensity.

Appendix C. Procedure for the Newton-Raphson solution

The procedure is summarised below using a superscript for the increments and a subscript for the iterations:

1. the starting equilibrium point is the homogeneous condition, because $\mathbf{u} = 0$ when no loads are applied. It is indicated by the superscript (0), thus:

$$(\mathbf{u}^{(0)} = 0, \lambda^{(0)} = 0) \quad \text{and} \quad \mathbf{g}^{(0)} = \mathbf{g}(\mathbf{u}^{(0)}, \lambda^{(0)}) = 0;$$

2. the tangent stiffness matrix is calculated for the initial condition:

$$\mathbf{K}_T^{(0)} = \left(\frac{d\mathbf{g}}{d\mathbf{u}} \right)^{(0)};$$

3. the first incremental solution (*predictor*) is calculated as

$$\mathbf{u}_0^{(1)} = \mathbf{u}^{(0)} + (\mathbf{K}_T^{(0)})^{-1} \Delta \mathbf{q}_e^{(1)},$$

where $\Delta \mathbf{q}_e^{(1)} = \lambda^{(1)} \mathbf{q}_{e1}$ and \mathbf{q}_{e1} is unitary reference load vector;

4. the function \mathbf{g} is calculated in the $(\mathbf{u}_0^{(1)}, \lambda^{(1)})$ condition,

$$\mathbf{g}_0^{(1)} = \mathbf{g}(\mathbf{u}_0^{(1)}, \lambda^{(1)}).$$

If $\mathbf{g}_0^{(1)} \neq 0$ and does not satisfy the convergence criterion of the predictor, the Newton-Raphson iterations begin for the load factor increment $\lambda^{(1)}$

- (a) the tangent stiffness matrix is calculated for $(\mathbf{u}_0^{(1)}, \lambda^{(1)})$:

$$\mathbf{K}_{T0}^{(1)} = \left(\frac{d\mathbf{g}}{d\mathbf{u}} \right)_0^{(1)};$$

- (b) the increment at the first iteration is then

$$\delta \mathbf{u}_1^{(1)} = -(\mathbf{K}_{T0}^{(1)})^{-1} \mathbf{g}_0^{(1)};$$

- (c) the solution at the first iteration is

$$\mathbf{u}_1^{(1)} = \mathbf{u}_0^{(1)} + \delta \mathbf{u}_1^{(1)};$$

- (d) if the function $\mathbf{g}_1^{(1)} = \mathbf{g}(\mathbf{u}_1^{(1)}, \lambda^{(1)}) \neq 0$ and does not satisfy the convergence criterion for the corrector, another iteration is needed;

- (e) the tangent stiffness matrix is calculated for $(\mathbf{u}_1^{(1)}, \lambda^{(1)})$:

$$\mathbf{K}_{T1}^{(1)} = \left(\frac{d\mathbf{g}}{d\mathbf{u}} \right)_1^{(1)};$$

- (f) the increment at the second iteration is

$$\delta \mathbf{u}_2^{(1)} = -(\mathbf{K}_{T1}^{(1)})^{-1} \mathbf{g}_1^{(1)};$$

- (g) the solution at the second iteration is

$$\mathbf{u}_1^{(1)} = \mathbf{u}_1^{(1)} + \delta \mathbf{u}_2^{(1)};$$

- (h) the function $\mathbf{g}_2^{(1)} = \mathbf{g}(\mathbf{u}_2^{(1)}, \lambda^{(1)})$ is calculated to check the convergence. The last n th iteration is the one for which $\mathbf{g}_n^{(1)}$ satisfies the corrector convergence criterion.

The second equilibrium point is then $(\mathbf{u}^{(1)}, \lambda^{(1)})$, where $\mathbf{u}^{(1)} = \mathbf{u}_n^{(1)}$. The procedure continues starting from point 1, but with $(\mathbf{u}^{(1)}, \lambda^{(1)})$ as initial condition and the load factor $\lambda = \lambda^{(2)}$.

Appendix D. Simplified model of MFC 8514-P1 actuators

Fig.[D.24] represents the section between two consecutive electrodes of the IDE of an MFC-P1 type piezoelectric transducer. The positive and the negative electrodes are spaced along the piezoelectric rod longitudinal direction. This arrangement establishes the d_{33} -operational mode, where both the direction of the electric field vector and the deformation of the transducer are parallel to the piezoelectric rod longitudinal direction (direction 3 in this case). The electric field component, Ξ_3 , for a given electric potential difference $\Delta V = \Xi_3 = -\Delta V/t_e$ and the axial strain of the section between the two electrodes is $\epsilon_3 = d_{33}E_3$.

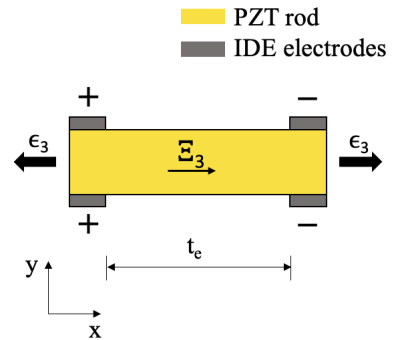


Figure D.24: Operational mode of a piezoelectric actuator with a d_{33} -coupling.

In an MFC 8514-P1 actuator there are 170 sections between the IDE electrodes, equally spaced with $t_e = 0.5$ mm, thus the axial strain of the actuator is:

$$\epsilon_x^{d_{33}-effect} = 170 \cdot d_{33}E_3. \quad (D.1)$$

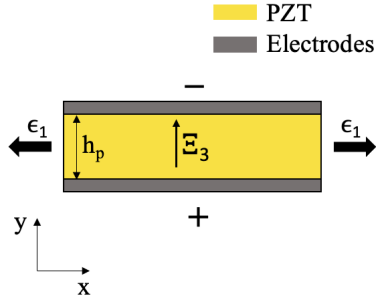


Figure D.25: Operational mode of a piezoelectric actuator with a d_{31} -coupling.

The electro-mechanical behaviour of the piezoelectric actuators considered in the new RZT model and described in Appendix B refers to the d_{31} -operational mode, where the positive and the negative electrodes are continuous layers placed one on the top and one on the bottom surface of the PZT. This arrangement causes a deformation of the actuator along the PZT longitudinal direction (called direction 1 in this operational mode), like the d_{33} -operational mode, but the electric field component, E_3 , is orthogonal to the PZT rod longitudinal direction. The electric field component, E_3 , for a given electric potential difference ΔV is $E_3 = -\Delta V/h_p$ and the axial strain of the actuator is:

$$\epsilon_x^{d_{31}-effect} = d_{31} \cdot E_3. \quad (D.2)$$

In order to model the MFC 8514-P1 actuator in a d_{31} -operational mode, the value of the piezoelectric coefficient d_{31} can be found assuming that the axial strain for a given electric potential difference ΔV has to be the same as the value obtained for the actual d_{33} -operational mode:

$$d_{31} = 170 \cdot d_{33} \frac{h_p}{t_e}. \quad (D.3)$$

The piezoelectric coefficient of the MFC 8514-P1 is $d_{33} = 4.6 \times 10^{-10}$ m/V, thus $d_{31} = 2.76 \times 10^{-10}$ m/V and the corresponding piezoelectric stress coefficient is $e_{31} = E_1 \cdot d_{31} = 8.40$ N/m/V, where E_1 is the Young modulus in the longitudinal direction of the piezoelectric material defined in Table [2].